RESEARCH ARTICLE

Formation of sea ice bridges in narrow straits in response to wind and water stresses

Bhargav Rallabandi[1] (ID), **Zhong Zheng[2,3,4]**, **Michael Winton[5]**, and **Howard A. Stone[1]**

[1]Department of Mechanical and Aerospace Engineering, Princeton University, Princeton, New Jersey, USA, [2]Department of Applied Mathematics and Theoretical Physics, University of Cambridge, Cambridge, UK, [3]BP Institute, University of Cambridge, Cambridge, UK, [4]Department of Earth Sciences, University of Cambridge, Cambridge, UK, [5]NOAA/Geophysical Fluid Dynamics Laboratory, Princeton, New Jersey, USA

Abstract Ice bridges are rigid structures composed of sea ice that form seasonally in the many straits and channels of the Canadian Arctic Archipelago. Driven primarily by atmospheric stresses, these ice bridges are formed when sufficiently thick ice "jams" during the course of its flow between land masses, resulting in a region of stationary compacted ice that is separated from a region of flowing open water (a polynya) by a static arch. Using a continuum description of sea ice that is widely used in climate modeling, we present an asymptotic theory of the process of formation of such bridges in slender channels when the motion of the ice is driven by external wind and water stresses. We show that for an arbitrary channel shape, ice bridges can only form within a range of ice properties that is determined by the channel geometry and the external stress. We then compare the results of our theory with direct numerical simulations and observational evidence. Finally, we provide simple analytical expressions for the mean velocity of the ice flow as a function of the channel shape, the properties of the ice, and the wind and water stresses along the channel.

Plain Language Summary Ice bridges are stationary structures that form in narrow straits due to a stoppage of sea ice flow. Such ice bridges connect the land masses that make up the strait and are important both for local climate and ecology. We develop a theory that exploits the slenderness of the straits, showing that the formation of an ice bridge can be understood using techniques commonly used to describe fluid flows. We find that ice bridges are formed only for a range of ice properties that depends on the shape of the strait and the forcing conditions. These insights on the flow of sea ice can aid climate modeling efforts and help interpret sea ice measurements in straits.

1. Introduction

An ice bridge is a stationary rigid structure comprising tightly packed sea ice that spans the width of a strait between two land masses and is formed during the regular course of the flow of sea ice through a strait. Often, such an ice bridge is separated from a large region of open water, i.e., a polynya, by a static arch. The motion of the ice leading to the formation of ice bridges in straits is typically driven by wind, as evidenced by field measurements [*Samelson et al.*, 2006]. Ice bridges are a seasonal occurrence in several parts of the Canadian Arctic Archipelago, e.g., in Nares Strait, and persist for several months through the Arctic winter. Over this time, the stationary ice field becomes landfast, stabilizing both the ice arch and the polynya [*Marsden et al.*, 2004]. Similar ice bridges to those in straits are also observed at the edge of the ice cover [*Scambos et al.*, 2009].

The formation and maintenance of stable ice bridges have two major consequences for local climate and ecology. First, the static nature of the ice arches impedes the further flow of sea ice through the strait from the Arctic Basin into the warmer Atlantic Ocean. The failure to establish an ice bridge can lead to the irrecoverable loss of multiyear Arctic sea ice and a significant increase in Arctic ice export [*Kwok et al.*, 2010; *Ryan and Münchow*, 2017]. Second, the polynyas that are formed downstream of the ice arches are crucial in regulating the exchange of gases and nutrients and have an increased uptake of solar energy, and therefore form regions of high ecological activity [*Stirling*, 1997; *Bowman and McCuaig*, 2003; *Hobson et al.*, 2002].

Thus, the failure to form an ice bridge can adversely affect ice export and the ecosystem on local, and possibly global, scales.

Despite their regular occurrence, the formation and breakup of ice bridges and their associated polynyas are not well understood and have been the topic of several studies. Observational efforts have characterized sea ice fluxes through straits [*Kwok*, 2005; *Samelson et al.*, 2006; *Kwok*, 2006; *Kwok et al.*, 2010] although a concurrent quantification of ice properties, fluxes and forcing conditions has proved to be challenging. Early theoretical studies adapted ideas from soil mechanics and the statics of granular materials in chutes [*Richmond and Gardner*, 1962] to the formation of ice bridges [*Sodhi*, 1977]. More recently, investigations into dynamical aspects of ice bridge formation and breakup have utilized continuum descriptions of sea ice rheology that are commonly employed in climate modeling [*Dumont et al.*, 2009; *Stelma*, 2015]. The formation of ice arches has also been observed in discrete-element simulations modeling the interactions between individual floes [*Rabatel et al.*, 2015].

The narrowness of most straits that exhibit ice bridge formation renders them below the resolution of typical global climate models (GCMs). However, it is precisely this geometric feature that lends itself to approximate analysis using techniques common to the study of fluid flow in channels. Here, we build upon our previous work [*Rallabandi et al.*, 2017] and develop a theoretical description of the flow of sea ice in a narrow strait in response to external wind and water stresses. The starting point for our theory is a continuum description of sea ice rheology, which has been an area of active research for several decades. Beginning with the work of *Coon et al.* [1974], *Rothrock* [1975a], and *Hibler* [1979], a number of rheological models for sea ice have been proposed, e.g., *Smith* [1983]; *Overland and Pease* [1988]; *Ip et al.* [1991]; *Tremblay and Mysak* [1997]. Comparisons between different rheological models in climate simulations can be found in *Ip et al.* [1991] and *Zhang and Rothrock* [2005]. For example, *Coon et al.* [2007] found that the anisotropic lead structure and the discontinuous nature of the ice field are important at length scales of $\sim$10 km. Recent research has sought to incorporate the effect of anisotropy [*Wilchinsky and Feltham*, 2011, 2006] due to lead formation, compressive shear faults [*Schulson*, 2004] and fracturing [*Hibler*, 2001; *Dansereau et al.*, 2016]. *Feltham* [2008] provides an overview of recent developments in the modeling of sea ice rheology.

In the present work, we use the viscous-plastic rheology of *Hibler* [1979], which is widely employed in climate simulations. As we show in subsequent sections, the theory rests on the general feature that the rheological behavior of sea ice depends on its physical properties. While we develop the theory using the rheology of *Hibler* [1979] (which is analytically tractable), the governing physical principles identified here are more general and can, in principle, be adapted to other rheological models. We obtain analytical predictions for the flux of sea ice and quantitative criteria for the formation of ice bridges that links the rheological properties of the ice to the geometry of the strait and the external forcing conditions. These theoretical predictions compare favorably against the results of direct numerical simulations. Our theory provides an analytic tool to describe the flow of sea ice in straits that can be used as an aid to observational studies, or as direct input to GCMs in cases where straits are too narrow to be resolved.

The article is organized as follows: section 2 sets up the problem and summarizes the rheological model of the sea ice that we use. In section 3, we develop an analytical description of the model by invoking the narrowness of the channel. The implications of our findings and comparisons to numerical simulations and observational data are discussed in section 4. Conclusions are presented in section 5.

2. Sea Ice Dynamics and Rheology

We consider the flow of sea ice through a narrow channel of characteristic half-width w_0 and length ℓ_0, as shown in Figure 1. The channel is assumed to be symmetric about $y = 0$ and has a prescribed shape $y = w(x)$. The motion of the ice is driven by an external atmospheric (wind) stress that acts on its top surface. Resistance to the flow of the ice occurs due to two main sources: (i) water drag due to relative motion between the ice and the ocean, and (ii) internal stresses due to the motion of the floes relative to each other and the rigid boundaries of the channel.

Here, we adopt the common approach in climate modeling of treating the ice field as a continuum, rather than considering the dynamics of individual ice floes. Then, the motion of the ice can be described by a
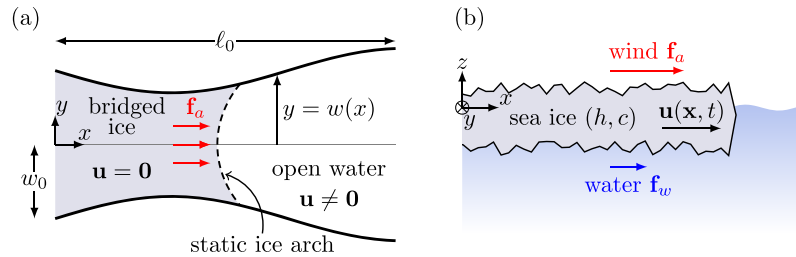
Figure 1. Motion of sea ice in response to atmospheric stresses $\mathbf{f}_a$ and oceanic stresses $\mathbf{f}_w$ in a strait of a given shape $w(x)$; the flow is described by a velocity field $\mathbf{u}(\mathbf{x}, t)$. (a) Top view of an ice bridge, showing stationary "bridged" ice separated from flowing open water by a static ice arch. Here, ℓ_0 and w_0 are the characteristic length and half-width, respectively, of the strait. (b) Side view of ice flow (not specific to ice bridges) indicating atmospheric and oceanic stresses. The ice field is two dimensional and is described by thickness and compactness fields $h(\mathbf{x}, t)$ and $c(\mathbf{x}, t)$, respectively.

two-dimensional velocity field $\mathbf{u}(\mathbf{x}, t) = u\mathbf{e}_x + v\mathbf{e}_y$, where $\mathbf{x}$ is a position vector in the plane of the ice flow, with z perpendicular to the plane and $\mathbf{e}_z$ the corresponding unit vector (see Figure 1). A balance of ice momentum in the plane of flow, obtained upon integrating the (3D) momentum equation through the ice thickness can then be written as

$$\rho_i^A \left(\frac{D\mathbf{u}}{Dt} + v_C \, \mathbf{e}_z \times \mathbf{u} \right) = \mathbf{f}_a + \mathbf{f}_w + \nabla \cdot \boldsymbol{\sigma}, \tag{1}$$

where D/Dt represents the material time derivative and v_C is the Coriolis frequency [*Trenberth*, 1992]. Here, $\rho_i^A(\mathbf{x}, t)$ is the areal density of the ice field (i.e., the total mass of ice per unit area), $\mathbf{f}_a$ is the atmospheric stress on its top surface, and $\mathbf{f}_w$ is the stress due to water flow relative to the ice, acting on its bottom surface. The quantity $\boldsymbol{\sigma}$ is the depth-integrated stress tensor of the ice, and therefore has units of force per length. While we will generally refer to $\boldsymbol{\sigma}$ as the internal stress in the ice, and $\mathbf{f}_a$ and $\mathbf{f}_w$ as stresses, it should be understood that the dimensions of $\boldsymbol{\sigma}$ differ that those of $\mathbf{f}_a$ and $\mathbf{f}_w$ by a unit of length. Gravitational forcing due to gradients of sea surface height are generally small and are neglected here [*Trenberth*, 1992].

The acceleration of the ice is typically only important on time scales of a few hours and is expected to play a small role in the formation of ice bridges, which occurs over a few days [*Rothrock*, 1975b; *Hibler et al.*, 2006; *Lepparanta*, 2011]. The Coriolis pseudoforce is ~0.01 Pa for meter-thick sea ice with a typical free-drift speed of ~0.1 ms^{-1}, and is even smaller for the slowly moving or stationary ice fields characteristic of bridge formation. By contrast, atmospheric stresses are typically ≳0.1 Pa, and thus form the dominant external driving mechanism. The influence of the Coriolis force is further suppressed in a narrow strait (even in the absence of ice bridges) since it acts primarily normal to the direction of flow, i.e., normal to land boundaries. Thus, it is appropriate to neglect both the acceleration and Coriolis terms in the momentum balance (1) for the purpose of describing the formation of ice bridges.

Atmospheric and water stresses depend, respectively, on the relative wind-ice and ocean-ice velocities. For simplicity, we will assume that the turning angles of wind and ocean currents are small, and thus write

$$\mathbf{f}_a = \rho_a C_{da} |\mathbf{u}_a - \mathbf{u}| (\mathbf{u}_a - \mathbf{u}) \quad \text{and} \tag{2a}$$

$$\mathbf{f}_w = \rho_w C_{dw} |\mathbf{u}_w - \mathbf{u}| (\mathbf{u}_w - \mathbf{u}), \tag{2b}$$

where ρ_a and ρ_w are air and water densities, respectively, $\mathbf{u}_a$ and $\mathbf{u}_w$ are their respective velocities, and C_{da} and C_{dw} are dimensionless drag coefficients [*McPhee*, 1975; *Trenberth*, 1992].

For typical ice speeds (~0.1 m·s^{-1}), the relative air-ice velocity is dominated by the wind velocity $\mathbf{u}_a$ (typically 5–10 m·s^{-1}). Thus, the wind stress is often taken to be independent of $\mathbf{u}$, see e.g., *Dumont et al.* [2009]. By contrast, the relative velocity between ice and water is usually considered to be dominated by the speed of the ice [*Trenberth*, 1992]. However, this latter approximation is clearly not appropriate when the velocity of the ice is zero, as is the case for ice bridge formation. Further, ocean currents can be appreciable in straits [*Samelson et al.*, 2006] and can in general play a role in the ice dynamics. Here, we focus on the case where $|\mathbf{u}| \ll |\mathbf{u}_w|$ and $|\mathbf{u}| \ll |\mathbf{u}_a|$, which is relevant to situations involving ice bridges. For simplicity, we assume that both air and water velocities are constant, spatially uniform and unidirectional along the channel axis,

and write $\mathbf{u}_a = u_a\mathbf{e}_x$, and $\mathbf{u}_w = u_w\mathbf{e}_x$. Neglecting contributions that are quadratic in the ice velocity, the wind and water stresses can be written as

$$\mathbf{f}_a = \rho_a C_{da} u_a |u_a| \mathbf{e}_x - \rho_a C_{da} |u_a| (2u\,\mathbf{e}_x + v\,\mathbf{e}_y) + \mathcal{O}(\rho_a C_{da}|\mathbf{u}|^2), \quad \text{and} \tag{3a}$$

$$\mathbf{f}_w = \rho_w C_{dw} u_w |u_w| \mathbf{e}_x - \rho_w C_{dw} |u_w| (2u\,\mathbf{e}_x + v\,\mathbf{e}_y) + \mathcal{O}(\rho_a C_{da}|\mathbf{u}|^2). \tag{3b}$$

The approximate expression for $\mathbf{f}_w$ remains valid as long as $|\mathbf{u}| \ll |\mathbf{u}_w|$, which in particular includes the case of ice-bridge formation. The assumption that along-strait wind stresses are dominant is borne out by observations [*Samelson et al.*, 2006] as well as by model reanalysis data [*Dumont et al.*, 2009] in Nares Strait; these findings suggest that the winds are not geostrophic, but are orographically funneled along the straits [*Kwok*, 2005]. We note that the effects of the small across-strait wind stresses (e.g., due to nonzero turning angles) on the transverse motion of the sea ice are further suppressed due to the geometric confinement of the ice by the land boundaries of the narrow strait.

Thus, the momentum equation (1) in the plane of the ice flow reduces to the stress balance

$$\nabla \cdot \boldsymbol{\sigma} + \mathbf{f} - \kappa_d \left(\mathbf{I} - \frac{1}{2}\mathbf{e}_y\mathbf{e}_y \right) \cdot \mathbf{u} = \mathbf{0}, \tag{4}$$

where $\mathbf{f} = f\mathbf{e}_x$, with

$$f = \rho_a C_{da} u_a |u_a| + \rho_w C_{dw} u_w |u_w|, \quad \text{and} \tag{5a}$$

$$\kappa_d = 2(\rho_a C_{da}|u_a| + \rho_w C_{dw}|u_w|). \tag{5b}$$

Here, f is an effective external driving stress and κ_d is a resistance with dimensions of stress per velocity, both of which are independent of the ice velocity $\mathbf{u}$. We will assume that $f > 0$ without loss of generality and $\kappa_d > 0$, so that the term linear in $\mathbf{u}$ in (4) corresponds to a drag that opposes the motion of the ice. For typical parameters $\left(C_{dw}/C_{da} = O(1),\ \rho_w/\rho_a \sim 10^3,\ |u_w/u_a| \lesssim 10^{-2} \right)$, the external stress f in (5a) is primarily due to wind and the drag κ_d in (5b) arises mainly due to the motion of water.

2.1. Overview of Sea Ice Rheology

We summarize *Hibler*'s [1979] model for sea ice, which is commonly used in climate modeling and is also adopted here. In this model, the sea ice is described as a two-dimensional viscous-plastic medium whose internal stress tensor $\boldsymbol{\sigma}$ is related to the rate of strain tensor $\mathbf{E} = \frac{1}{2}(\nabla\mathbf{u} + \nabla\mathbf{u}^T)$ by the constitutive law

$$\boldsymbol{\sigma} = -p\,\mathbf{I} + \eta(\alpha^2 - 1)(\mathrm{tr}\,\mathbf{E})\,\mathbf{I} + 2\eta\,\mathbf{E}, \tag{6}$$

where α is an $\mathcal{O}(1)$ dimensionless parameter. The depth-integrated viscosity η has units of force per length per strain rate, depends on both p and E, and is defined as

$$\eta \equiv \frac{1}{\alpha^2} \max\left\{ \frac{p}{\max(E^*, E)}, \zeta_{\min} \right\}. \tag{7}$$

Here, E^* is a dimensionless constant with units of strain rate, and E is an invariant measure of $\mathbf{E}$ that is defined by

$$E \equiv \frac{1}{\alpha}\sqrt{2\,\mathrm{tr}\,(\mathbf{E}\cdot\mathbf{E}) + (\alpha^2-1)(\mathrm{tr}\,\mathbf{E})^2} = \frac{1}{\alpha}\left\{ \left(\frac{\partial u}{\partial y} + \frac{\partial v}{\partial x}\right)^2 + \left(\frac{\partial u}{\partial x} - \frac{\partial v}{\partial y}\right)^2 + \alpha^2\left(\frac{\partial u}{\partial x} + \frac{\partial v}{\partial y}\right)^2 \right\}^{1/2}. \tag{8}$$

Also, $\zeta_{\min}$ is a constant with the same dimensions as η; we note from (7) that $\zeta_{\min}/\alpha^2$ sets the smallest allowed value of η. It is noted that the ice pressure p, the yield curve eccentricity α, the strain rate tensor $\mathbf{E}$ and its invariant measure E defined here are usually expressed as $P/2$, e, ϵ and Δ, respectively, in the literature [*Hibler*, 1979; *Hunke*, 2001].

The plastic part of the rheology, for which $\eta = p/(\alpha^2 E)$ in (7), is obtained under the assumption that plastic stresses in the ice lie on an elliptic yield curve with eccentricity α in principal stress space. The magnitude of the yield curve (in stress space) is set by p, which governs the overall magnitude of internal stress. The relationship between plastic stress and strain rate is then obtained by assuming an associated flow rule [*Hibler*,

1977]. We remark that for a purely plastic material, $\boldsymbol{\sigma}$ is invariant to a rescaling of $\boldsymbol{E}$ ($\eta \propto E^{-1}$). The plastic rheology must therefore be regularized for large and small E, implemented in the constitutive law through the parameters E^* and $\zeta_{\min}$, respectively, in (7). This model is qualitatively similar to models of dense granular flows in that p sets the scale of both normal and shear stresses by controlling the scale of the viscosity η [*Jop et al.*, 2006; *Forterre and Pouliquen*, 2008; *Henann and Kamrin*, 2013].

The thickness distribution of the ice [*Thorndike et al.*, 1975; *Toppaladoddi and Wettlaufer*, 2015] is approximated by a two-level sea ice model [*Trenberth*, 1992]. The mean thickness of the sea ice $h(\mathbf{x}, t)$ (also called the effective thickness) is defined so that $\rho_A = h\rho_i$, where ρ_i is the volumetric mass density of the ice, which is assumed constant; thus $h(\mathbf{x}, t)$ is a proxy for the areal density of the ice field. We also consider the evolution of a compactness field $c(\mathbf{x}, t)$, which is defined as the fraction of area covered by rheologically significant "thick" ice relative to the total ice cover. The ice field can evolve due to a combination of mechanical and thermodynamic processes. The characteristic time scale for an $\mathcal{O}(1)$ change in ice thickness due to mechanical aggregation is $\tau_m \approx |\nabla \cdot \mathbf{u}|^{-1} \approx 20$ days, assuming a typical length scale of $\sim$200 km and an ice velocity of $\sim$0.1 m $\cdot$ s^{-1} [*Samelson et al.*, 2006]. On the other hand, the a similar change in ice thickness due to freezing seawater takes a typical time $\tau_f = \rho_i L h^2 / (\kappa(T_a - T_f))$, where L is the latent heat of fusion per volume, κ is the thermal conductivity of sea ice, T_a is the atmospheric temperature and T_f is the freezing temperature of seawater [*Leppäranta*, 2011; *Worster and Rees Jones*, 2015]. For a typical value of $\rho_i L / \kappa \approx 0.2\,^\circ$C $\cdot$ day $\cdot$ cm^{-2} [*Leppäranta*, 2011], a temperature difference $(T_a - T_f) \sim 20\,^\circ$C characteristic of Nares Strait [*Ryan and Münchow*, 2017], and meter-thick ice, we find $\tau_f \approx 90$ days. Observations indicate that the growth of stationary (landfast) ice due to freezing is further impeded by the insulating snow cover, suggesting an even longer thermodynamic time scale of $\tau_f \approx 180$ days [*Howell et al.*, 2016].

Thus, thermodynamic growth of ice is subdominant to mechanical rearrangement of floes on the time scales of a few days, over which an ice bridge begins to form from an initially flowing state. Neglecting thermodynamic processes, the conservation equations for h and c are

$$\frac{\partial h}{\partial t} + \nabla \cdot (\mathbf{u}h) = 0 \tag{9a}$$

$$\frac{\partial c}{\partial t} + \nabla \cdot (\mathbf{u}c) = 0, \quad \text{subject to} \quad 0 \leq c \leq 1. \tag{9b}$$

The constraint $0 \leq c \leq 1$ is explicitly included to prevent fully compact ice from being further compacted by a converging velocity field ($\nabla \cdot \mathbf{u} < 0$). We note that the seasonal stability of ice bridges does ultimately depend on thermodynamic processes; for example, ice bridges are stabilized by the freezing of interstitial ocean water between mechanically jammed floes, and break up at the beginning of the melt season as the ice thins [*Kwok et al.*, 2010; *Ryan and Münchow*, 2017]. We do not model these processes here but instead focus on the conditions that are necessary for the initiation of ice bridges, i.e., the mechanical jamming of initially flowing ice.

Finally, it is necessary to relate p to h and c. Given that p represents a depth-integrated stress, it scales approximately linearly with h [*Coon et al.*, 1974; *Wilchinsky and Feltham*, 2004; *Feltham*, 2008]. Further, the ice can support stresses only when the compactness c is close to unity. In less compact ice, the interactions between individual floes is weak and stresses are not transmitted effectively across the entire field. These observations motivate a relationship of the form

$$p = She^{-k(1-c)}, \tag{10}$$

where S is a strength parameter with units of force per area, and k is a numerical constant. This completes the description of the rheological model of *Hibler* [1979], which depends on h and c of the ice. The strength parameter S is identical to the quantity $P^*/2$ in the literature [*Hunke and Dukowicz*, 1997; *Dumont et al.*, 2009]. Typical values of key physical and rheological parameters are listed in Table 1. As discussed in section 1, several other sea ice models exist in the literature [e.g., *Ip et al.*, 1991; *Zhang and Rothrock*, 2005; *Feltham*, 2008; *Wilchinsky and Feltham*, 2011; *Dansereau et al.*, 2016]. The key general feature of all of these models, including the one that is used here (i.e., that of *Hibler* [1979]), is that the ice properties are tied to the pressure p, which enters the momentum balance both as an average normal stress and through shear stresses via the rheology.

Equations (4–10) represent a nonlinear system for the unknowns $\boldsymbol{u}$, $\boldsymbol{\sigma}$, p, h and c, which are functions of $\boldsymbol{x}$ and t and depend the shape of the channel $w(x)$ and the parameters α, ζ_{min}, E^* and k. The problem can be solved given appropriate initial and boundary conditions on h and c and boundary conditions on $\boldsymbol{u}$. Here, we assume that the flow satisfies no-slip at the walls of the channel:

$$\boldsymbol{u}=\boldsymbol{0} \quad \text{at} \quad y=\pm w(x) . \tag{11}$$

We note that a nonzero slip velocity between the ice field and land boundaries may be possible in general, in particular for a rarified (noncompact) ice field. However, the condition of no-slip at the boundaries is self-evidently satisfied for ice bridge conditions, where the ice is stationary in the strait (including at land boundaries) [*Kwok et al.*, 2010; *Ryan and Münchow*, 2017]. By continuity, the no-slip condition is likely to apply in the dynamical processes leading up to the formation of such ice bridges. The no-slip condition is also supported by the existence of substantial regions of coastal, nonmoving, landfast sea ice in the Canadian Arctic Archipelago, see e.g., *Howell et al.* [2016].

The problem is generally time-dependent through the continuity equations (9a), although the simplified stress balance (4) is quasi-static. Nonlinearities enter both through the dependence of η on E in (7), as well as the dependence of p on h and c given in (10). We note here that ζ_{min}, which was originally introduced by *Hibler* [1979] as a means to suppress numerical instabilities, plays the more important *physical* role of preventing η from vanishing in the limit $p/E \to 0$. Such a regularization of η for large strain rates is necessary on physical grounds for the flow to satisfy the no-slip condition (11), as we show in subsequent sections. The value of the limiting viscosity ζ_{min} is not well constrained on physical grounds [*Hibler*, 1979; *Dumont et al.*, 2009]. The analysis that we develop in subsequent sections provides a means by which to constrain ζ_{min} and other model parameters using independent observational data. We return to this point toward the end of section 4 and discuss the role of ζ_{min} in greater detail.

Owing to the complicated rheology of the ice field, the system of equations is typically solved numerically. Here, we develop a formalism that is valid for long and slender channels and obtain an analytical expression for the ice velocity as a function of the local ice properties. We then apply the analytical result to obtain averaged one-dimensional continuity equations for h and c, and show that the theory makes quantitative predictions for the formation of ice bridges. Although these averaged continuity equations must be solved numerically in general, they are significantly simpler than the full two-dimensional system. As we will show in the following sections, the formation of ice bridges follows from two key model features: (i) the rheology depends on the ice properties, and (ii) the plastic rheology is regularized for large values of the strain-rate measure E, which is necessary in order for the flow to satisfy no-slip conditions on the walls of the channel.

2.2. Dimensionless Problem Statement for a Narrow Channel

To aid the analysis that follows, it is useful to first recast the problem exactly in terms of dimensionless variables appropriate to the geometry at hand. We define a characteristic aspect ratio of the channel (see Figure 1),

$$\delta \equiv \frac{w_0}{\ell_0} \ll 1 , \tag{12}$$

which is assumed small (typical of straits where ice bridges are observed) and will serve as the basis for the analysis we develop here. Motivated by long-wave approximations for Bingham plastic flows [*Balmforth and Craster*, 1999] and lubrication flows of viscous fluids [*Ockendon and Ockendon*, 1995], we introduce the dimensionless variables (accented quantities)

$$\tilde{x} \equiv \frac{x}{\ell_0}, \quad \tilde{y} \equiv \frac{y}{w_0}, \quad \tilde{u} \equiv \frac{u}{u_0}, \quad \tilde{v} \equiv \frac{v}{\delta u_0}, \quad \tilde{p} \equiv \frac{p}{p_0} \quad \text{and} \quad \tilde{\eta} = \frac{\eta}{\zeta_{min}/\alpha^2}, \tag{13}$$

where the pressure scale p_0 and velocity scale u_0 must be determined; the scale for η follows directly from (7).

Assuming that the balance of stress in (4) is primarily between the external stress $\boldsymbol{f}$ and transverse gradients of shear stress results in the velocity scale

$$u_0 = \frac{\alpha^2 w_0^2 f}{\zeta_{min}} . \tag{14}$$

Next, we recognize that in order to sustain both a finite flow speed and the no-slip condition at the walls of the channel, the flow must (at least in some region near the walls) behave viscously and attain its minimum

viscosity $\eta=\zeta_{min}/\alpha^2$, cf. (7). This minimum viscosity is realized only when $p/E<\zeta_{min}$, as is evident from (7). Observing from (8) that $E=O(u_0/(\alpha w_0))$, the above condition sets a relevant pressure scale

$$p_0=\frac{\zeta_{min}u_0}{\alpha w_0}=\alpha w_0 f\,. \tag{15}$$

Under the rescaling for velocities and lengths, the strain rate measure E in (8) can be cast in dimensionless form as

$$\tilde{E}\equiv\frac{E}{E_0}=\left\{\left(\frac{\partial\tilde{u}}{\partial\tilde{y}}+\delta^2\frac{\partial\tilde{v}}{\partial\tilde{x}}\right)^2+\delta^2\left(\frac{\partial\tilde{u}}{\partial\tilde{x}}-\frac{\partial\tilde{v}}{\partial\tilde{y}}\right)^2+\delta^2\alpha^2\left(\frac{\partial\tilde{u}}{\partial\tilde{x}}+\frac{\partial\tilde{v}}{\partial\tilde{y}}\right)^2\right\}^{1/2}, \tag{16}$$

where $E_0\equiv u_0/(\alpha w_0)$ is the characteristic scale of E.

The dimensionless viscosity $\tilde{\eta}$ follows from (7), (13) and (16) as

$$\tilde{\eta}=\frac{\eta}{\zeta_{min}/\alpha^2}=\max\left\{\frac{\tilde{p}}{\max(\tilde{E}^*,\tilde{E})},1\right\} \tag{17}$$

where $\tilde{E}^*\equiv E^*\alpha w_0/u_0=E^*\zeta_{min}/(\alpha w_0 f)$. For the typical values of $E^*=2\times10^{-9}$ s^{-1}, $f=0.2$ Pa, $\alpha=2$ and $w_0=25$ km [*Dumont et al.*, 2009], we find $\tilde{E}^*\approx10^{-5}$. This exceedingly small ratio will ultimately not enter the analysis that we develop and may be set to zero in principle, but is required for a numerical treatment of the equations for small strain rates [*Hunke*, 2001]. By contrast, the regularization of the plastic rheology for large strain rates (effected through ζ_{min}) is important, since a flow with zero viscosity cannot satisfy no-slip conditions.

The dimensionless stress balance (4) with (5) can then be written in its component form as

$$\delta\frac{\partial}{\partial\tilde{x}}\left\{-\alpha\tilde{p}+\delta\tilde{\eta}\left((\alpha^2+1)\frac{\partial\tilde{u}}{\partial\tilde{x}}+(\alpha^2-1)\frac{\partial\tilde{v}}{\partial\tilde{y}}\right)\right\}+\frac{\partial}{\partial\tilde{y}}\left\{\tilde{\eta}\left(\frac{\partial\tilde{u}}{\partial\tilde{y}}+\delta^2\frac{\partial\tilde{v}}{\partial\tilde{x}}\right)\right\}-\beta^2\tilde{u}+1=0\,, \tag{18a}$$

$$\frac{\partial}{\partial\tilde{y}}\left\{-\alpha\tilde{p}+\delta\tilde{\eta}\left((\alpha^2-1)\frac{\partial\tilde{u}}{\partial\tilde{x}}+(\alpha^2+1)\frac{\partial\tilde{v}}{\partial\tilde{y}}\right)\right\}+\delta\frac{\partial}{\partial\tilde{x}}\left\{\tilde{\eta}\left(\frac{\partial\tilde{u}}{\partial\tilde{y}}+\delta^2\frac{\partial\tilde{v}}{\partial\tilde{x}}\right)\right\}-\delta\frac{\beta^2}{2}\tilde{v}=0\,, \tag{18b}$$

where

$$\beta^2\equiv\frac{\alpha^2 w_0^2\kappa_d}{\zeta_{min}} \tag{19}$$

is the dimensionless ratio of drag to internal stresses. Here, we only concern ourselves with positive drag coefficients $\beta^2>0$ (i.e., $\kappa_d/f>0$), so that the drag opposes the motion of the ice. Note that $\beta\to0$ corresponds to limit where internal stresses are dominant in balancing wind stress, while $\beta\to\infty$ corresponds to the free-drift balance (balance of wind and water stresses) with a linear drag law.

The equation of state (10) for p takes the dimensionless form

$$\tilde{p}=\tilde{h}e^{-k(1-c)},\quad\text{where}\quad\tilde{h}=\frac{h}{\alpha w_0 f/S}, \tag{20}$$

with $\tilde{h}$ being the dimensionless effective ice thickness. Defining $\tilde{t}=t/(\ell_0/u_0)$, the rescaled continuity equations for $\tilde{h}$ and c are

Table 1. Typical Values of Key Parameters[a]

Parameter	Symbol	Value
Ice-water drag coefficient	C_{dw}	3.2×10^{-3}
Ice-air drag coefficient	C_{da}	$\approx2\times10^{-3}$
Elliptic yield curve eccentricity	α	$0<\alpha\leq2$
Lower-bound bulk viscosity	ζ_{min}	0.4 GPa·m·s
Lower-bound strain rate for plastic rheology	E^*	2×10^{-9} s^{-1}
Ice strength parameter	S	13.75 kPa
Pressure-compactness decay exponent	k	20

[a]Taken from *Dumont et al.* [2009].

Table 2. Relevant Characteristic Scales and Dimensionless Parameters

Physical Quantity	Characteristic Scale	Dimensionless Variable
Axial distance	ℓ_0	$\tilde{x} = \dfrac{x}{\ell_0}$
Transverse distance	w_0	$\tilde{y} = \dfrac{y}{w_0}$
Axial velocity	$u_0 \equiv \dfrac{\alpha^2 w_0^2 f}{\zeta_{\min}}$	$\tilde{u} = \dfrac{u}{u_0}$
Transverse velocity	$v_0 \equiv \dfrac{w_0 u_0}{\ell_0}$	$\tilde{v} = \dfrac{v}{v_0}$
Time	$t_0 \equiv \dfrac{\ell_0}{u_0}$	$\tilde{t} = \dfrac{t}{t_0}$
Strain rate invariant	$E_0 \equiv \dfrac{u_0}{\alpha w_0}$	$\tilde{E} = \dfrac{E}{E_0}$
Effective thickness	$h_0 \equiv \dfrac{\alpha w_0 f}{S}$	$\tilde{h} = \dfrac{h}{h_0}$
Pressure	$p_0 \equiv \alpha w_0 f$	$\tilde{p} = \dfrac{p}{p_0} = \tilde{h} e^{-k(1-c)}$
Shear viscosity	$\dfrac{\zeta_{\min}}{\alpha^2}$	$\tilde{\eta} = \dfrac{\eta}{\zeta_{\min}/\alpha^2}$
Aspect ratio (dimensionless)		$\delta \equiv \dfrac{w_0}{\ell_0}$
Linear drag parameter (dimensionless)		$\beta \equiv \sqrt{\dfrac{\alpha^2 w_0^2 \kappa_d}{\zeta_{\min}}}$
Lower-bound strain-rate for plastic rheology (dimensionless)		$\tilde{E}^* = \dfrac{E^*}{E_0}$

$$\frac{\partial \tilde{h}}{\partial \tilde{t}} + \frac{\partial(\tilde{u}\tilde{h})}{\partial \tilde{x}} + \frac{\partial(\tilde{v}\tilde{h})}{\partial \tilde{y}} = 0 \quad \text{and} \tag{21a}$$

$$\frac{\partial c}{\partial \tilde{t}} + \frac{\partial(\tilde{u}c)}{\partial \tilde{x}} + \frac{\partial(\tilde{v}c)}{\partial \tilde{y}} = 0 , \quad \text{with} \quad 0 \le c \le 1. \tag{21b}$$

This scaling of time ensures that $\mathcal{O}(1)$ dimensionless times correspond to advection along the characteristic channel length.

The dimensionless problem described by (12–21) is an exact rescaling of the equations in section 2, and involves the channel shape $\tilde{w}(\tilde{x}) = w(x)/w_0$, dimensionless parameters α, β, δ, $\tilde{E}^*$ and k, and the dimensionless functions $\tilde{u}$, $\tilde{v}$, $\tilde{p}$, $\tilde{h}$ and c, which depend on $\tilde{x}$, $\tilde{y}$ and $\tilde{t}$. The definitions of the relevant characteristic scales and dimensionless variables are summarized in Table 2.

3. Long-Wave Theory for Flow Through a Strait

The dimensionless system of equations in section 2.2 can now be analyzed in the limit of narrow channels, i.e., $\delta \ll 1$ using techniques similar to those of *Rallabandi et al.* [2017]. First, we note that the rheology has a similar structure to that of a Bingham plastic fluid in that the constitutive law has a plastic part ($\eta \propto E^{-1}$) with viscous regularizations for large and small E [*Bird et al.*, 1977]. A large body of literature exists on the flow of *incompressible* Bingham fluids in narrow channels [*Tichy*, 1991; *Balmforth and Craster*, 1999; *Frigaard and Ryan*, 2004]. The particular situation of ice flow differs from classical Bingham plastic flows since (i) the ice flow is not incompressible in the *xy* plane, (ii) the viscosity η of the ice depends not only on E but also on p, and (iii) the pressure p is coupled to the advection of the ice properties h and c.

Nevertheless, the spatial structure of the ice flow in straits is similar to that of traditional incompressible plastic fluids and can be analyzed using the techniques developed in *Balmforth and Craster* [1999]. We show that as a general feature, the flow of the ice consists of viscous shear layers near the walls of the channel, and a plastic flow region near the middle of the channel. The flows in these two regions can be analyzed by means of a perturbation expansion in the small parameter δ [cf. *Rallabandi et al.*, 2017]. In the next two sections, we focus on developing a description of the horizontal velocity field in terms of the ice properties using the method of matched asymptotic expansions. We then use this result in the advection equations for h and c to determine the evolution of the ice field.

3.1. Viscous Shear Layer

In general, the flow can only be no-slip at the channel walls by behaving viscously in a region near the walls, see e.g., *Balmforth and Craster* [1999] and *Frigaard and Ryan* [2004]. Due to the symmetry of the problem, it is sufficient to consider only $\tilde{y} \geq 0$. By definition, the viscous region near $\tilde{y} = \tilde{w}$ has $\tilde{\eta} = \tilde{\eta}_v = 1$, where the subscript v will henceforth be used to denote properties of the ice field in the viscous layer. Thus, to leading order in δ, the stress balances in (18) reduce to

$$\frac{\partial}{\partial \tilde{y}} \left(\tilde{\eta}_v \frac{\partial \tilde{u}_v}{\partial \tilde{y}} \right) - \beta^2 \tilde{u}_v + 1 = 0 \quad \text{and} \quad \frac{\partial \tilde{p}_v}{\partial \tilde{y}} = 0 . \tag{22a,b}$$

Integrating (22b), we find that $\tilde{p}_v$ is independent of $\tilde{y}$, and so write $\tilde{p}_v = \tilde{p}_v(\tilde{x})$. We note that all flow quantities are generally time dependent, although we will often avoid writing the explicit dependence of the variables on $\tilde{t}$ for notational convenience.

Due to (17), the condition $\tilde{p}_v / \tilde{E}_v < 1$ must persist throughout the viscous region, where $\tilde{\eta} = \tilde{\eta}_v = 1$. For small δ, we can use (16) to approximate this condition as

$$\tilde{E}_v \approx \left| \frac{\partial \tilde{u}_v}{\partial \tilde{y}} \right| > \tilde{p}_v. \tag{23}$$

By definition, the internal boundary that separates the viscous layer from regions of plastic flow corresponds to the onset of failure of the above condition, i.e., where $\tilde{E}_v = \tilde{p}_v$. We denote the location of this inner boundary of the viscous layer by some yet unknown curve $\tilde{y} = \tilde{y}_v(\tilde{x}, \tilde{t})$, so that $\tilde{E} = \tilde{p}_v$ on $\tilde{y} = \tilde{y}_v(\tilde{x}, \tilde{t})$; see (23). Equation (22a) can now be integrated subject to the boundary conditions

$$\tilde{u}_v = 0 \quad \text{at} \quad \tilde{y} = \tilde{w} \quad \text{and} \tag{24a}$$

$$\left| \frac{\partial \tilde{u}_v}{\partial \tilde{y}} \right| = \tilde{p}_v \quad \text{at} \quad \tilde{y} = \tilde{y}_v \tag{24b}$$

to obtain

$$\tilde{u}_v(\tilde{x}, \tilde{y}) = \frac{\cosh \beta(\tilde{w} - \tilde{y}_v) - \cosh \beta(\tilde{y} - \tilde{y}_v) + \beta \tilde{p}_v \sinh \beta(\tilde{w} - \tilde{y})}{\beta^2 \cosh \beta(\tilde{w} - \tilde{y}_v)} , \tag{25}$$

which is valid for $\tilde{y} \in (\tilde{y}_v, \tilde{w})$. The pressure $\tilde{p}_v(\tilde{x}, \tilde{t})$ is determined by the ice properties $\tilde{h}$ and c through the constitutive law (20). However, the location of the yield surface $\tilde{y}_v(\tilde{x}, \tilde{t})$ is unknown at this point in the analysis (see Figure 2a for a sketch of the idea) and must be determined to complete the description of the flow.

3.2. Central Plastic Flow Region and Matching

In the central part of the channel where $|\tilde{y}| < \tilde{y}_v$, the viscous solution (25) is no longer valid, in particular due to the sufficiently low strain rates ($\tilde{E} < \tilde{p}$) in this region for the flow to realize *plastic* behavior. Since both shear and extensional components of the rate-of-strain tensor are generally comparable for a plastic flow, it is necessary to analyze the stress balance in this region using perturbation techniques. Following *Balmforth and Craster* [1999], we use the expansions

$$\tilde{u}(\tilde{x}, \tilde{y}) = \tilde{u}_p(\tilde{x}) + \delta \, \tilde{u}_{p1}(\tilde{x}, \tilde{y}) + \mathcal{O}(\delta^2) , \tag{26a}$$

$$\tilde{v}(\tilde{x}, \tilde{y}) = \tilde{v}_p(\tilde{x}, \tilde{y}) + \mathcal{O}(\delta) , \tag{26b}$$

$$\tilde{p}(\tilde{x}, \tilde{y}) = \tilde{p}_p(\tilde{x}, \tilde{y}) + \mathcal{O}(\delta) , \tag{26c}$$

where the subscript p denotes quantities in the plastic flow region. The particular expansion of $\tilde{u}(\tilde{x}, \tilde{y})$ in (26a) is consistent with the condition that shear strain rates are not the dominant mode of deformation in the plastic flow region.

The longitudinal component of velocity is nearly independent of $\tilde{y}$, i.e., $\tilde{u} \approx \tilde{u}_p(\tilde{x})$ in the plastic flow region but varies along the channel. Due to this feature, the plastic flow region is also referred to as the "pseudo-plug" flow region and the internal boundary between viscous and plastic flows $\tilde{y} = \tilde{y}_v$ as the "pseudo-yield
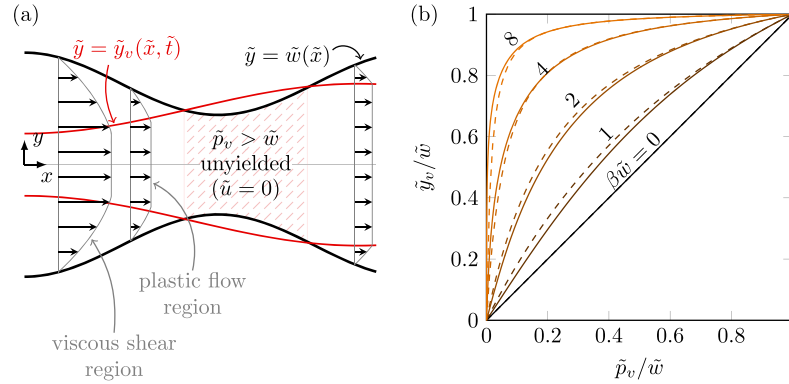
Figure 2. (a) Sketch of ice flow in a channel of typical shape $\tilde{w}(\tilde{x})$, indicating the pseudo-yield surface $\tilde{y}_v(\tilde{x})$ and velocity profiles (arrows) at different sections. The flow in any channel section is generically divided by the pseudo-yield surface into a central plastic flow region and viscous shear layers near the walls. If the ice pressure exceeds a critical value ($\tilde{p}_v > \tilde{w}$ in dimensionless terms), viscous layers cannot be supported and the flow is locally stationary (shaded region). (b) Yield surface location $\tilde{y}_v/\tilde{w}$ as a function of $\tilde{p}_v/\tilde{w}$ for several $\beta\tilde{w}$. Solid lines represent exact solutions of (32), which are computed numerically. Dashed lines are the predictions of (34), which are formally valid when $|\tilde{y}_v/\tilde{w} - 1| \ll 1$ but provide a good approximation to the exact solutions over the entire range of $\tilde{y}_v$. Note that $\tilde{y}_v = \tilde{p}_v$ when $\beta = 0$.

surface" [*Balmforth and Craster*, 1999]. Continuity of horizontal velocity across the pseudo-yield surface enforces that

$$\tilde{u}_p(\tilde{x}) = \tilde{u}_v(\tilde{x}, \tilde{y}_v(\tilde{x})), \tag{27}$$

which is accurate up to $\mathcal{O}(\delta)$ terms. Using (25) and (27), we have thus obtained approximate expressions for the horizontal velocity in both the viscous and plastic flow regions as a function of $\tilde{p}_v$, $\tilde{w}$ and $\tilde{y}_v$.

To complete the description of the horizontal flow, we are tasked with finding the position of the pseudo-yield surface $\tilde{y}_v(\tilde{x})$. To this end, we consider the balance of stresses (18) in the plastic flow region. Using the expansions (26) for the velocity components, the strain rate measure $\tilde{E}$ in (16) can be written, to leading order in δ, as $\tilde{E} = \delta\tilde{E}_p$ where

$$\tilde{E}_p = \sqrt{\left(\frac{\partial\tilde{u}_{p1}}{\partial\tilde{y}}\right)^2 + \left(\frac{\partial\tilde{u}_p}{\partial\tilde{x}} - \frac{\partial\tilde{v}_p}{\partial\tilde{y}}\right)^2 + \alpha^2\left(\frac{\partial\tilde{u}_p}{\partial\tilde{x}} + \frac{\partial\tilde{v}_p}{\partial\tilde{y}}\right)^2} \tag{28}$$

carries contributions from both shear and extension rates in the plastic flow region. Substituting the expression (28) into the definition (17) of $\tilde{\eta}$ then results in $\tilde{\eta} = \tilde{\eta}_p/\delta$, where $\tilde{\eta}_p \equiv \tilde{p}_p/\tilde{E}_p$. We remark that the detailed expression for $\tilde{E}_p$ is not essential in obtaining the leading-order results for the horizontal velocity below, but enters the expression for the transverse velocity $\tilde{v}_p$ (see Appendix A).

Substituting (26) into (18), the balance of stresses in the plastic region is

$$\frac{\partial}{\partial\tilde{y}}\left(\tilde{\eta}_p\frac{\partial\tilde{u}_{p1}}{\partial\tilde{y}}\right) - \beta^2\tilde{u}_p + 1 = 0 \tag{29a}$$

$$\frac{\partial}{\partial\tilde{y}}\left(-\alpha\tilde{p}_p + \tilde{\eta}_p\left((\alpha^2 - 1)\frac{\partial\tilde{u}_p}{\partial\tilde{x}} + (\alpha^2 + 1)\frac{\partial\tilde{v}_p}{\partial\tilde{y}}\right)\right) = 0. \tag{29b}$$

We note that (29) remains unchanged in physical meaning from (22); (29a) constitutes a balance between transverse shear stress gradients, wind stress and drag, while (29b) states that $\boldsymbol{\sigma} : \mathbf{e}_y\mathbf{e}_y$ is uniform across the channel. Applying the condition of zero shear stress at $\tilde{y} = 0$ (which is a consequence of the symmetry of the channel and the forcing), recognizing that $\tilde{u}_p$ is independent of $\tilde{y}$, and integrating (29a) yields

$$\tilde{\eta}_p\frac{\partial\tilde{u}_{p1}}{\partial\tilde{y}} = -(1 - \beta^2\tilde{u}_p)\tilde{y}, \tag{30}$$

which describes the shear stress in the ice in the plastic flow region. In addition to the continuity of horizontal velocity used to obtain (27), the shear stresses in the flow must also be continuous across the pseudo-yield surface, which can be written as

$$\tilde{\eta}_p \frac{\partial \tilde{u}_{p1}}{\partial \tilde{y}} = \tilde{\eta}_v \frac{\partial \tilde{u}_v}{\partial \tilde{y}} \qquad \text{at} \quad \tilde{y} = \tilde{y}_v \,, \tag{31}$$

where we recall that $\tilde{\eta}_v = 1$. On substituting the expressions (25), (27) and (30) into (31), we obtain an implicit expression for $\tilde{y}_v(\tilde{x})$:

$$\frac{\tilde{y}_v}{\tilde{w}} \left(\frac{1 - (\beta \tilde{w}) \frac{\tilde{p}_v}{\tilde{w}} \sinh \beta \tilde{w} \left(1 - \frac{\tilde{y}_v}{\tilde{w}} \right)}{\cosh \beta \tilde{w} \left(1 - \frac{\tilde{y}_v}{\tilde{w}} \right)} \right) = \frac{\tilde{p}_v}{\tilde{w}}. \tag{32}$$

The above expression can be solved numerically (we use *MATLAB*'s numerical root finding algorithm) to obtain a solution for the yield surface $\tilde{y}_v(\tilde{x})$ of the form $\tilde{y}_v/\tilde{w} = \mathcal{F}(\tilde{p}_v/\tilde{w}, \beta \tilde{w})$, indicated as solid curves in Figure 2b.

The flow structure described above relies on the existence of the viscous layer in the region $\tilde{y}_v(\tilde{x}) < \tilde{y} < \tilde{w}(\tilde{x})$. Thus, only solutions of (32) for which $\tilde{y}_v < \tilde{w}$ are physically relevant. It is clear from (32) that the limiting case $\tilde{y}_v = \tilde{w}$, which corresponds to vanishingly thin viscous layers, occurs only when $\tilde{p}_v = \tilde{w}$ (i.e., when $\tilde{y}_v \to = \tilde{p}_v > \tilde{w}_v$), as shown in Figure 2b. If $\tilde{p}_v > \tilde{w}$ ($\leftrightarrow \tilde{y}_v > \tilde{w}_v$) at some location $\tilde{x}$ along the channel, a viscous layer cannot be supported locally. In this case, the flow is locally unyielded can only satisfy no-slip at the channel walls if $\tilde{u} = \tilde{v} = 0$ across the entire local cross section of the channel (see Figure 2a). This criterion $\tilde{p}_v > \tilde{w}$ for locally arrested flow establishes a link between rheology and geometry which, as we will show in subsequent sections, is crucial to the formation of ice bridges. It is noted that the same criterion was obtained by *Rallabandi et al.* [2017] for the special case of $\beta = 0$ (no water drag); here we have shown that this result applies independent of the water drag ($\beta \neq 0$).

The cases of plastic, viscous and unyielded flow can be written together as

$$\tilde{u}(\tilde{x}, \tilde{y}) = \begin{cases} \tilde{u}_p(\tilde{x}) = \tilde{u}_v(\tilde{x}, \tilde{y}_v) & \text{for} \quad 0 < \tilde{y} < \tilde{y}_v(\tilde{x}) \\[2ex] \tilde{u}_v(\tilde{x}, \tilde{y}) & \text{for } \tilde{y}_v(\tilde{x}) \leq \tilde{y} < \tilde{w}(\tilde{x}) \\[2ex] 0, & \end{cases} \begin{array}{l} \\[2ex] , \text{ for } \tilde{p}_v(\tilde{x}) < \tilde{w}(\tilde{x}), \quad (33a) \\[2ex] \text{for } \tilde{p}_v(\tilde{x}) \geq \tilde{w}(\tilde{x}) \quad (33b) \end{array}$$

Solving (32) for $\tilde{y}_v$, which can then be used to compute both $\tilde{u}_v$ and $\tilde{u}_p$ via (25) and (27), completes the description of the horizontal ice velocity. The instantaneous horizontal velocity given by (33) is sketched in Figure 2a for a typical channel shape $\tilde{w}(\tilde{x})$ and pseudo-yield surface $\tilde{y} = \tilde{y}_v(\tilde{x})$; note that the flow is symmetric about $\tilde{y} = 0$.

While a numerical solution of (32) is generally necessary, we can obtain approximate solutions in the limit of narrow viscous layers, i.e., $\tilde{w} - \tilde{y}_v \ll 1$. Using a Taylor expansion of (32) about $\tilde{y}_v = \tilde{w}$ up to linear order in $(\tilde{w} - \tilde{y}_v)$, we find

$$\tilde{y}_v \approx \tilde{w} \left(1 - \frac{1 - \frac{\tilde{p}_v}{\tilde{w}}}{1 + (\tilde{w}\beta)^2 \frac{\tilde{p}_v}{\tilde{w}}} \right), \qquad \text{valid for} \quad 1 - \frac{\tilde{y}_v}{\tilde{w}} \ll 1 \,. \tag{34}$$

Although (34) is formally valid when $\tilde{w} - \tilde{y}_v \ll 1$ (or equivalently when $\tilde{w} - \tilde{p}_v \ll 1$), it compares well with numerical solutions of (32) for arbitrary $\tilde{p}_v$ and β, as indicated by the dashed lines in Figure 2b. It can be shown that (34) is asymptotic at leading order for both $\beta \ll 1$ and $\beta \gg 1$ by analyzing (32). Thus, this approximate expression for $\tilde{y}_v$ can be used along with (25) and (33) to obtain a closed-form analytic expression for the horizontal velocity as a function of the pressure distribution $\tilde{p}_v(\tilde{x})$ and the channel shape $\tilde{w}(\tilde{x})$.

Integrating the $\tilde{y}$-component of the stress balance in the plug flow region (29b) yields expressions for $\tilde{v}_p$ (cf. Appendix A), although this result does not enter the analysis of the advection of ice properties $(\tilde{h}, c)$ that we consider presently. We also note that in case of locally arrested (i.e., unyielded) flow, which occurs for $\tilde{p}_v > \tilde{w}$, a more careful consideration of the rheology (17) results in $\tilde{u} = \mathcal{O}(\tilde{E}^*)$ and $\tilde{v} = \mathcal{O}(\tilde{E}^*)$. However, the value of $\tilde{E}^*$ is sufficiently small for typical parameters that it can be set to zero in practice.

3.3. Averaged Equations for Ice Advection
The expressions for the horizontal velocity obtained above can now be used in the advection problem for the evolution of $\tilde{h}$ and c. Rather than solving the full two-dimensional equations (21), we obtain a simplified

one-dimensional system in terms of averaged quantities by integrating (21) between $\tilde{y} = -\tilde{w}(\tilde{x})$ and $\tilde{y} = \tilde{w}(\tilde{x})$. Recognizing that $\tilde{u} = \tilde{v} = 0$ at both of these limits due to the no-slip condition (11), the averaged equations are

$$\frac{\partial(\tilde{w}\langle\tilde{h}\rangle)}{\partial\tilde{t}} + \frac{\partial(\tilde{w}\langle\tilde{u}\tilde{h}\rangle)}{\partial\tilde{x}} = 0 \quad \text{and} \tag{35a}$$

$$\frac{\partial(\tilde{w}\langle c\rangle)}{\partial\tilde{t}} + \frac{\partial(\tilde{w}\langle\tilde{u}c\rangle)}{\partial\tilde{x}} = 0\,, \quad \text{with} \quad 0 \leq c \leq 1, \tag{35b}$$

where the average across the channel is defined as $\langle(\cdot)\rangle \equiv \frac{1}{2\tilde{w}(\tilde{x})}\int_{-\tilde{w}(\tilde{x})}^{\tilde{w}(\tilde{x})}(\cdot)\,\mathrm{d}\tilde{y}$.

The averaged equations (35) are an exact rewriting of the two-dimensional advection equations (21) and do not involve the velocity component normal to the channel axis, but now contain averaged quantities $\langle\tilde{h}\rangle$, $\langle c\rangle$, $\langle\tilde{u}\tilde{h}\rangle$ and $\langle\tilde{u}c\rangle$. Contingent upon appropriate initial conditions, we now make the approximation that both $\tilde{h}$ and c are nearly uniform across the channel for all $\tilde{t}$. This approximation is consistent with both field observations and numerical simulations of ice bridges [*Melling*, 2002; *Dumont et al.*, 2009; *Stelma*, 2015], for which variations of the ice field across the channel are typically small far away from the location of the arch. Under this assumption, the pressure $\tilde{p}$ is also uniform across the channel and can be written as $\tilde{p}(\tilde{x},\tilde{t}) = \tilde{h}e^{-k(1-c)} \approx \tilde{p}_v$, where we henceforth understand that $\tilde{h} \approx \tilde{h}(\tilde{x},\tilde{t})$ and $c \approx c(\tilde{x},\tilde{t})$. Hereafter, we will also suppress the subscript v on $\tilde{p}_v$ for notational convenience and write $\langle\tilde{h}\rangle \approx \tilde{h}$, $\langle c\rangle \approx c$, $\langle\tilde{u}\tilde{h}\rangle = \langle\tilde{u}\rangle\tilde{h}$ and $\langle\tilde{u}c\rangle = \langle\tilde{u}\rangle c$. The averaged advection equations (35a) then take the form

$$\frac{\partial(\tilde{w}\,\tilde{h})}{\partial\tilde{t}} + \frac{\partial(\tilde{w}\,\langle\tilde{u}\rangle\tilde{h})}{\partial\tilde{x}} = 0 \quad \text{and} \tag{36a}$$

$$\frac{\partial(\tilde{w}\,c)}{\partial\tilde{t}} + \frac{\partial(\tilde{w}\,\langle\tilde{u}\rangle c)}{\partial\tilde{x}} = 0\,, \quad \text{with} \quad 0 \leq c \leq 1. \tag{36b}$$

The mean velocity $\langle\tilde{u}\rangle$ can be computed from (25) and (33) as

$$\langle\tilde{u}\rangle = \frac{1}{\tilde{w}\beta^3}\left\{\tilde{w}\beta\left(1 + \frac{\tilde{p}}{\tilde{w}}\right) - \tilde{w}\beta\left(\frac{\tilde{p}}{\tilde{w}} + \frac{\tilde{y}_v}{\tilde{w}}\right)\mathrm{sech}\left[\beta\tilde{w}\left(1 - \frac{\tilde{y}_v}{\tilde{w}}\right)\right] - \left(1 - \left(\beta\tilde{w}\right)^2\frac{\tilde{p}}{\tilde{w}}\frac{\tilde{y}_v}{\tilde{w}}\right)\tanh\left[\beta\tilde{w}\left(1 - \frac{\tilde{y}_v}{\tilde{w}}\right)\right]\right\}, \tag{37}$$

where we recall that $\tilde{p} = \tilde{h}e^{-k(1-c)}$. The above expression can be evaluated given $\tilde{y}_v$, which can be obtained either by solving (32) numerically or by using the approximate expression (34). Thus, we have obtained a closed system of coupled one-dimensional advection equations for $\tilde{h}$ and c, where the coupling occurs through $\langle\tilde{u}\rangle$. This reduced-order system (36, 37) can be solved numerically and presents a significant simplification over the full 2D dynamics.

4. Discussion

The averaged advection equations (36a) form a coupled one-dimensional quasi-linear hyperbolic system for the evolution of $\tilde{h}$ and c, in which the coupling occurs through the mean flow speed $\langle\tilde{u}\rangle$, given by (37), and the pressure $\tilde{p} = \tilde{h}e^{-k(1-c)}$. We recall that the mean flow speed becomes identically zero when $\tilde{p} > \tilde{w}$ (which corresponds to $\tilde{y}_v > \tilde{w}$) for *arbitrary* values of the damping parameter β, cf. (34, 37). We solve the system (36) using the so-called Harten–Lax–van Leer method [*Harten et al.*, 1983], which is a mass-conserving finite-volume method that accounts for the local direction of wave propagation [*LeVeque*, 2002]. Here, we compute these characteristic directions analytically (see Appendix B), although they can also be computed numerically.

Before presenting the numerical results of the one-dimensional model (36), we note that its steady state solutions correspond to a constant flux of ice mass, $\tilde{w}\langle\tilde{u}\rangle\tilde{h} = \text{const.}$, and a constant flux of area covered by thick ice, $\tilde{w}\langle\tilde{u}\rangle c = \text{const.}$; we recall that $\tilde{h}$ is by definition the mass of ice per unit area per ice density. In particular, if we consider solutions with *zero* steady-state flux ($\tilde{w}\langle\tilde{u}\rangle\tilde{h} = \tilde{w}\langle\tilde{u}\rangle c = 0$), we find two possible families of solutions: The first corresponds to thick and compact ice with zero mean velocity ($\tilde{h}e^{-k(1-c)} > \tilde{w}$, $\langle\tilde{u}\rangle = 0$), while the second kind of steady-state solution corresponds to flowing open water

($\tilde{h}=c=0$, $\langle \tilde{u} \rangle > 0$). It follows that any step change between these two states is also a steady-state solution of (36) with zero flux, suggesting that the averaged equations admit solutions consistent with ice bridges.

4.1. Ice Advection in the Reduced-Order Model

As a conceptually and mathematically simple limit for which to present solutions of (36), we focus on the case of weak drag ($\beta \ll 1$), where the external stress $\boldsymbol{f}$ is balanced primarily by the internal stresses in the ice. We note that some of the features of the ice advection problem for the case of $\beta = 0$ (negligible water drag) were discussed in *Rallabandi et al.* [2017]. Here we discuss these features in greater depth and in addition show that the reduced-order theory generally allows for the formation of multiple ice bridges in channels. We then derive a criterion for ice bridge formation that that is applicable for arbitrary β. Quantitative results for the dependence of the mean ice velocity on β are discussed in subsequent sections.

In the limit $\beta \to 0$, the location of the pseudo-yield surface assumes the particularly simple form $\tilde{y}_v = \tilde{p}_v$, which is an exact solution of (32) in this limit. The mean velocity $\langle \tilde{u} \rangle$ in this limit is readily obtained from (37) as [*Rallabandi et al.*, 2017]

$$\langle \tilde{u} \rangle = \max \left\{ \frac{\tilde{w}^2}{3} \left(1 - \left(\frac{\tilde{p}}{\tilde{w}} \right)^3 \right), 0 \right\}, \tag{38}$$

where it is immediately clear that $\tilde{p} > \tilde{w}$ results in zero mean flow. Our numerical solutions of (36) confirm the above argument, and also elucidate the mechanism by which some initial conditions can evolve toward ice bridge solutions at steady state. For simplicity, we consider initially uniform ice properties

$$\tilde{h}(\tilde{x}, \tilde{t}=0) = \tilde{h}_i, \quad c(\tilde{x}, \tilde{t}=0) = c_i, \tag{39}$$

where $\tilde{h}_i$ and c_i are constants, but allow the channel shape $\tilde{w}(\tilde{x})$ to be nonuniform. Further, we focus on initially compact ice $c_i = 1$ and study the behavior of the solutions for different h_i. We denote the initial pressure by $\tilde{p}_i = \tilde{h}_i e^{-k(1-c_i)}$, noting that $\tilde{p}_i = \tilde{h}_i$ for $c_i = 1$. We also specify $\tilde{h}(\tilde{x}=0, \tilde{t}>0) = h_i$ and $c(\tilde{x}=0, \tilde{t}>0) = c_i$ as inlet boundary conditions, which represents a constant influx of ice at known properties. The same conditions on h and c are used at the outlet, although outlet conditions are less consequential to the solution due to the wave-like nature of the system (36); see also Appendix B.

We find three broad classes of qualitatively different time-dependent solutions of (36). The first of these corresponds to the case where $\tilde{p}_i < \tilde{w}(\tilde{x})$ everywhere in the channel, and is depicted in Figure 3a. In this case, $\langle \tilde{u} \rangle > 0$ at $\tilde{t}=0$ throughout the channel. As the ice field evolves, its properties $\tilde{h}$ and c redistribute throughout the channel, eventually reaching a steady state with nonzero constant fluxes of $\tilde{h}$ and c.

The second type of steady state which is depicted in Figure 3b, occurs for initial conditions in which $p_i > \tilde{w}(\tilde{x})$ in a part of the channel, and $\tilde{p}_i < \tilde{w}(\tilde{x})$ in the remainder of the channel. The region in which $\tilde{p}_i > \tilde{w}(\tilde{x})$ has zero local flow according to (38), and constitutes a local blockage (region between dashed lines in Figure 3b), while $\langle \tilde{u} \rangle > 0$ in the rest of the channel. The part of the flow upstream of the initial blockage advects ice toward the blocked region, causing it to thicken and pile up, which in the process increases $\tilde{p}$. This piling up continues until $\tilde{p}$ becomes locally equal to $\tilde{w}$, at which point the viscous layer becomes arbitrarily thin and causes the incoming flow to become arrested near the rear of the initial blockage. This process continues until the entire ice field upstream of the blockage has piled up sufficiently to stop flowing. By contrast, the flow downstream of the initial blockage flows unimpeded under the external stress, leaving behind ice that becomes thinner and less compact over time. The combination of the two processes results in the formation of a discontinuity in ice properties with zero steady state flux, $\tilde{w}\langle \tilde{u} \rangle \tilde{h} = \tilde{w}\langle \tilde{u} \rangle c = 0$. This behavior represents the one-dimensional analog of observed bridge formation events (summarized in Figure 3c), in which stationary thick ice is separated from a polynya (open water) by a static arch; here the arch is represented by the discontinuity. The above mechanism for ice bridge formation is insensitive to channel shape. Figure 3d shows flow in a channel with two constrictions, forming two ice bridges from initially uniform ice properties. Here, the flow of ice away from the upstream blockage accumulates at the downstream blockage during the process of bridge formation. We note that multiple ice bridges are often observed in Nares Strait [*Kwok et al.*, 2010; *Ryan and Münchow*, 2017].
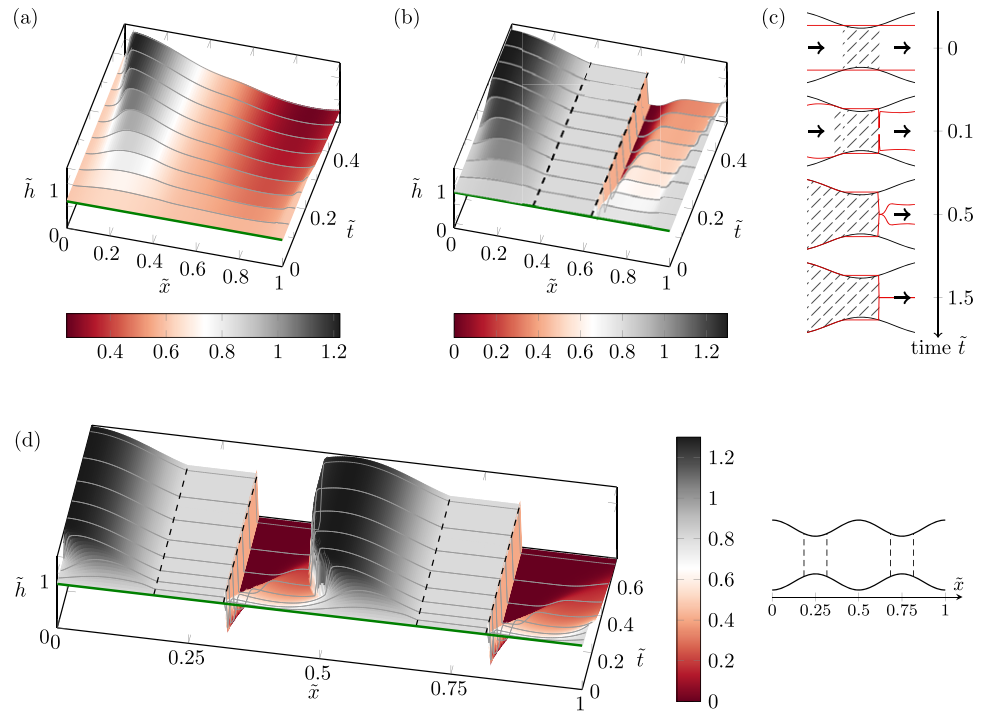
Figure 3. (a–c) Time-dependent solutions of the reduced-order model (36) for initial conditions $\tilde{h}=h_i$ and $c=c_i=1$, in a channel with $\tilde{w}(\tilde{x})=1+0.3\cos(2\pi\tilde{x})$, no water drag ($\beta=0$) and $k=20$. Panel (a) corresponds to the condition $\tilde{p}_i < \tilde{w}$ everywhere in the channel, and results in a steady-state solution with flow throughout the channel. Panel (b) corresponds to a case where $\tilde{p}_i > \tilde{w}$ in a part of the channel (the region between the dashed lines), which constitutes a local blockage. Incoming ice upstream of the blockage piles up and eventually becomes arrested, while ice downstream of the blockage flows and leaves behind open water; the combination of these processes forms an ice bridge. Colors in Figures 3a and 3b correspond to thick (gray) or thin (red) ice (as indicated by the colorbars), with $\tilde{h}(\tilde{x},\tilde{t})$ at different times indicated as gray curves and the uniform initial thickness indicated as a green horizontal line. Panel (c) indicates snapshots of the flow corresponding to different times in Figure 3b, indicating the yield surface $\tilde{y}=\tilde{y}_v(\tilde{x},\tilde{t})$ as a red curve, regions of nonzero velocity (arrows), and stationary parts of the flow (shaded). (d) Flow in a channel with two constrictions ($\tilde{w}(\tilde{x})=1+0.3\cos(4\pi\tilde{x})$, sketched on the right) but with the same conditions as in Figure 3b. This results in two ice bridges at steady state; multiple ice bridges are often observed in Nares Strait [*Ryan and Münchow*, 2017].

The third class of steady-state solution is relatively trivial and corresponds to the case in which $\tilde{p}_i > \tilde{w}(\tilde{x})$ *everywhere* in the channel. Here, the ice is too thick to flow through even the widest part of the channel at $\tilde{t}=0$. As a result, the flow remains at a zero-flux steady state for all times.

The three qualitatively different solutions correspond to initial conditions for either fully flowing, fully arrested or ice bridge solutions. The conditions discussed above can be stated slightly differently for a channel with maximum half-width w_{max} and minimum half-width w_{min}. The case $\tilde{p}_i < w_{min}/w_0$ results in flow everywhere in the channel, while the case $\tilde{p}_i > w_{max}/w_0$ corresponds to no flow anywhere in the channel. For intermediate pressures $w_{min}/w_0 < \tilde{p}_i < w_{max}/w_0$, parts of the ice field can flow ($\tilde{p}_i < \tilde{w}(\tilde{x})$ locally), while parts of it are arrested and never flow ($\tilde{p}_i > \tilde{w}(\tilde{x})$ locally). The combination of flowing and arrested states is a key feature of ice bridges, which are characterized by stationary compact ice upstream of flowing open water. Thus, in dimensional terms, the critical condition for the formation of ice bridges is

$$\frac{\alpha w_{min} f}{S} < h_i e^{-k(1-c_i)} < \frac{\alpha w_{max} f}{S}. \tag{40}$$

The above theoretical prediction follows directly from the critical condition for local arrested flow $\tilde{p} > \tilde{w}$. We emphasize that the condition for locally arrested flow is therefore not limited to $\beta=0$, but is generally applicable for any β, by virtue of (32) and (37).

Thus, the theoretical prediction (40) for the formation of ice bridges is borne out exactly by numerical simulations of the reduced-order system (36, 37) for *arbitrary* values of β. The inclusion of a quadratic drag law does not change the above result since terms proportional to $|\mathbf{u}|^2$ become subdominant to internal stresses

as the ice velocity approaches zero in a bridge formation scenario. The detailed time evolution of the ice field is closely related to wave propagation in the hyperbolic system (36) and is discussed in Appendix B.

As discussed in section 2.1, the reduced-order system (36) and the criterion (40) involve only mechanical changes of the ice field and exclude thermodynamic processes freezing or melting. We reemphasize the distinction between the mechanical formation of ice bridges and their long-term (seasonal) stability. The present study focuses on the mechanical processes involved in the formation of an ice bridge from a state of flow. Over the life span of the bridge (typically a few months [*Ryan and Münchow*, 2017]), freezing and melting become increasingly important [*Stelma*, 2015] (see also section 2.1), so that the stability of the bridge is no longer a simple function of the initial properties as in the criterion (40). We note that thermodynamic processes can be readily included within the present theoretical framework by introducing source or sink terms in (36) without modifying the expressions for the velocity developed in section 3, which involve only the balance of mechanical stresses. Thus, an analogous criterion to (40) that uses *instantaneous* (rather than initial) ice properties may still prove useful in assessing the seasonal stability of ice bridges.

4.2. Direct Numerical Simulations

We verify the results of our reduced-order analytical model against direct numerical simulations (DNS) of the dimensionless system of equations (12)–(21). The simulations are carried out by the use of the "elastic–viscous–plastic" (EVP) implementation of the sea ice rheology [*Hunke and Dukowicz*, 1997; *Hunke*, 2001], in which the constitutive law (6) is modified to include a numerical elasticity term. This modification allows for the use of longer time steps and approaches the true constitutive law (6) iteratively. In addition, the numerical description also includes inertia in the momentum balance (see equation (1)), which permits an explicit solution of the nonlinear momentum equations. A large number of subcycles (i.e., iterations) of the EVP rheology and the momentum equations are used for each physical time step in the simulation, see *Hunke and Dukowicz* [1997] for a detailed discussion. The results of the simulation are insensitive to changing the magnitude of the numerical elasticity and the size of the inertial term relative to internal stresses, verifying that these numerical modifications do not affect the results of the simulation.

We conduct simulations with uniform initial ice properties ($\tilde{h} = \tilde{h}_i$ and $c = c_i$ at $\tilde{t} = 0$) in a channel of nonuniform width $\tilde{w}(\tilde{x})$. As in the case of the numerical solution of the simplified system (36), we use boundary conditions corresponding to $\tilde{h} = \tilde{h}_i$ and $c = c_i$ at both the inlet and the outlet. In addition, we impose zero normal velocity gradient at the outlet, and no-slip at land boundaries. The number of subcycles in the EVP scheme is $N = 384$, the grid corresponds to 40 grid cells at the narrowest part of the channel and the elasticity parameter (E_o in *Hunke and Dukowicz* [1997]) is set to 0.25 for all the results presented here. We verify that the simulations are insensitive to both spatial and temporal resolution.

We fix $c_i = 1$ and vary $\tilde{h}_i$ for a fixed channel shape $\tilde{w}(\tilde{x})$ focusing on critical conditions for arch formation. For each value of h_i, we vary both the applied stress f in the range 0.1 Pa–0.4 Pa and the yield curve eccentricity α between 0.6 and 2. For the results discussed presently, we fix the drag parameter at $\beta = 0$; a discussion of the results for $\beta \neq 0$ is presented in subsequent sections. We find that all three flow regimes described in the previous section by the one-dimensional averaged equations occur in the direct numerical simulations, depending on the initial ice properties. These findings are consistent with previous numerical studies [*Dumont et al.*, 2009; *Stelma*, 2015]. Figure 4a shows a comparison between the theoretical criterion (40) and the results of the direct numerical simulation for a range of external forcing strengths f, yield ellipse eccentricities α, and initial heights h_i; see also *Rallabandi et al.* [2017]. The dynamics leading up to the formation of an ice bridge in DNS are shown in Figure 4b. The mechanism of ice bridge formation predicted by the reduced-order model (cf. Figures 3b and 3c) is in agreement with the results of DNS in Figure 4b. We use values of δ in the range of 1–10; Figure 4a uses this entire range of values, while Figure 4b is a representative simulation for $\delta = 1$.

We find good agreement between the predictions of the theory and the results of the full numerical simulations. We remark that the theory generally underpredicts the minimum thickness required for ice bridge formation, since it is developed under the assumption that flow features along the channel vary on a length scale $\ell_0 \gg w_0$. However, as the ice pack opens up downstream of the initial blockage, gradients of the ice field in both the $\tilde{x}$ and $\tilde{y}$ directions become comparable due to the generally two-dimensional structure of the arch [*Sodhi*, 1977; *Richmond and Gardner*, 1962]; see also Figure 4b. A more detailed treatment of the flow must also take into account the continuity of velocity and normal stresses *across* the arch and requires a fully two-dimensional analysis of the stress balances. This may partly explain why the ice bridges are
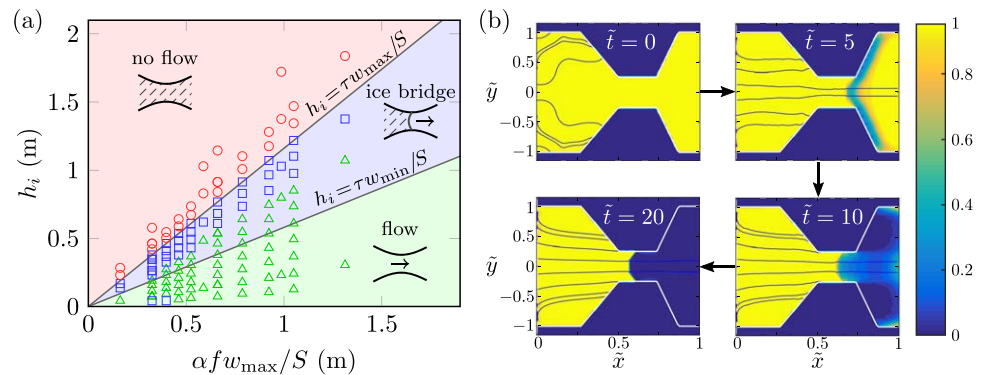
Figure 4. (a) Phase diagram showing numerical and theoretical results for the steady-state structure of the ice field as a function of the initial ice thickness h_i and the dimensional thickness scale $\alpha f w_{max}/S$. The initial concentration is $c_i = 1$ and the drag parameter is $\beta = 0$ in both the theory and the simulations. Results of the direct numerical simulations are indicated as symbols and the theoretical prediction (40) are shown as shaded regions. The steady state corresponds to free flow (triangles, green shading), completely arrested flow (circles, red shading) or ice bridge formation (squares, blue shading). Both theory and simulations correspond to $w_{max} = 2w_{min} = 50$ km and rheological parameters in Table 1. (b) Typical time-evolution of the ice field in DNS leading to ice bridge formation starting from uniform ice properties with constant rightward wind stress and zero water drag in a channel with $w_{max} = 4w_{min} = 100$ km and $\delta = 2$, indicating the compactness field $c(\boldsymbol{x}, t)$ (color) and instantaneous streamlines (curves); each unit of dimensionless time $\tilde{t}$ represents ≈ 2 days. Initially, the throat is too thin to allow ice to flow. Then, ice downstream of the throat, where the channel is wider, flows and opens up a growing region of open water. Subsequently, incoming ice upstream of the throat piles up, thereby forming an ice bridge. Note the similarities with the bridge-formation process in the reduced-order model, cf. Figures 3b and 3c.

observed for slightly greater initial thicknesses than the minimum thickness bounds predicted by the reduced-order model, see Figure 6a. Nonetheless, the present theory captures many of the features of the simulations and provides simple quantitative criteria (40) for arch formation.

4.3. Dependence of Ice Fluxes and Mean Velocities on β

We now consider the dependence of the mean ice velocity $\langle \tilde{u} \rangle$ on the drag parameter β defined in (19). Our aim is to build on results developed in previous sections to develop closed-form approximations for the mean velocity as a function of the channel geometry, forcing conditions and sea ice properties. These results are compared with both direct numerical simulations and observational data.

In the limit of both uniform channel widths and spatially uniform initial ice properties, the expressions for the velocity field in (33) and the discussion of the yield surface are exact statements up to errors of $\mathcal{O}(\tilde{E}^*)$. Equation (37) provides a general expression for the mean velocity for a given wind speed, drag β, pressure $\tilde{p}$ and the local width $\tilde{w}$ of the channel. The velocity profile and the mean velocity depend on the position of the pseudo-yield surface $\tilde{y}_v$, which is obtained as the solution to (32), in terms of $\tilde{w}$, $\tilde{p}$ and β. Figure 5 shows the rescaled average speed $\langle \tilde{u} \rangle / \tilde{w}^2$ as a function of $\tilde{p}/\tilde{w}$ for different values of $\beta \tilde{w}$ (solid curves).
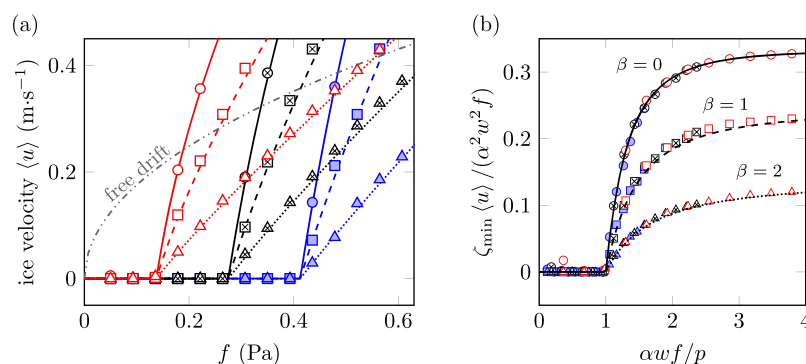
Figure 5. Rescaled mean velocity $\langle \tilde{u} \rangle / \tilde{w}^2$ as a function of $\tilde{p}/\tilde{w}$ for several values of $\beta \tilde{w}$. Solid lines represent exact solutions obtained by first solving (32) numerically for $\tilde{y}_v$ and substituting the result into (37). Dashed lines are the predictions of the approximate expression (42), which is asymptotic for $\beta \ll 1$ and $\beta \gg 1$ to leading order, and provides a good approximation to the exact solutions over the entire range of β. The flow is arrested when $\tilde{p} > \tilde{w}$ independent of the value of β. We recall that in dimensional terms, $\langle \tilde{u} \rangle / \tilde{w}^2 = \langle u \rangle \zeta_{min}/(\alpha^2 w^2 f)$, $\tilde{p}/\tilde{w} = p/(\alpha w f)$ and $\beta \tilde{w} = \sqrt{\alpha^2 w^2 \kappa_d/\zeta_{min}}$.

Consider limiting values of the mean velocity for small and large β. By using Taylor expansions of (37) in these limits and the approximate form of $\tilde{y}_v(\tilde{x})$ given in (34), which is asymptotic to leading order for both $\beta \ll 1$ and $\beta \gg 1$, we obtain

$$\langle \tilde{u} \rangle = \begin{cases} \max\left[\dfrac{\tilde{w}^2}{3}\left(1-\left(\dfrac{\tilde{p}}{\tilde{w}}\right)^3\right),0\right] & \text{for} \quad \beta \ll 1, \qquad (41a) \\[2em] \max\left[\dfrac{1}{\beta^2}\left(1-\dfrac{\tilde{p}}{\tilde{w}}\right),0\right] & \text{for} \quad \beta \gg 1. \qquad (41b) \end{cases}$$

The $\beta \ll 1$ limit was discussed in section 3.3 and was used to obtain the numerical solutions to the reduced-order (1D) system of equations (36) that are plotted Figures 3 and 4. The $\beta \gg 1$ asymptote corresponds to the situation in which the main stress balance occurs between the wind stress and water drag and the viscous layer is only required to enforce the no-slip condition at the channel walls. We construct a uniformly valid approximation for arbitrary β as twice the harmonic mean of the two limits in (41) to obtain

$$\langle \tilde{u} \rangle \approx \max\left[\tilde{w}^2 \left\{ \frac{1-\left(\frac{\tilde{p}}{\tilde{w}}\right)^3}{3 + (\beta\tilde{w})^2\left(1+\frac{\tilde{p}}{\tilde{w}}+\left(\frac{\tilde{p}}{\tilde{w}}\right)^2\right)} \right\}, 0\right]. \qquad (42)$$

Figure 5 shows the approximate expression (42) for $\langle \tilde{u} \rangle$ (dashed lines) as a function of $\tilde{p}/\tilde{w}$ for different values of $\beta\tilde{w}$. This approximation compares well with the exact expression (37) of $\langle \tilde{u} \rangle$, which can be evaluated subject to numerically solving (32). In dimensional terms, (42) can be written as

$$\langle u \rangle \approx \max\left[f\left\{ \frac{1-\left(\frac{p}{\alpha wf}\right)^3}{\frac{3\zeta_{min}}{\alpha^2 w^2} + \kappa_d\left(1+\frac{p}{\alpha wf}+\left(\frac{p}{\alpha wf}\right)^2\right)} \right\}, 0\right], \qquad (43)$$

thus providing a straightforward way to compute the mean ice velocity in the strait as a function of its geometry, the ice properties, and the wind and water stresses. The area flux of ice is, by definition, equal to $q = 2w\langle u \rangle$. Thus, the two limits of small and large β correspond to flows where internal stresses and water drag, respectively, balance the external wind stress. For intermediate values of β, the flux depends on both κ_d and ζ_{min}. Further, we observe from (43) that the mean velocity is quadratic in the width of the channel for narrow channels (internal stresses dominate; $\beta \ll 1$) and is independent of channel width for wider channels (surface drag dominates; $\beta \gg 1$). The limit of $\beta \gg 1$ corresponds to free drift, where the mean velocity is set by the balance between wind stress and water drag ($\langle u \rangle \sim f/\kappa_d$) in the limit of low ice strength ($p \ll \alpha wf$). Note that a quadratic drag law with a static ocean results in a velocity scale $\langle u \rangle_{quad} \sim \sqrt{f_a/(\rho_w C_{dw})}$ in the weak-ice limit ($p \ll \alpha wf$).

In Figure 6, we compare the predictions of our approximate expression (43) for the mean ice velocity with direct numerical simulations for a range of ice properties, external forcing conditions and linear drag coefficients. The theory is in excellent agreement with numerical simulations over the entire relevant parameter range, and accurately predicts both the critical wind stress for ice motion and the velocity (and by extension, the flux) of sea ice as a function of its properties. The present theory is applicable as long as the predicted velocities are smaller than the free-drift velocity obtained from a quadratic water drag. The algebraic simplicity of (43) allows it to be applied to the estimation of ice properties under measured forcing condition and ice fluxes through straits (or vice-versa) without the need for detailed simulations.

Figure 7 compares the predictions of our approximate theory for the mean velocity (43) with the data of *Samelson et al.* [2006] in Nares Strait, in which ice speeds along the strait were measured, and the wind stresses was computed from an atmospheric model. The wind stress and ice speed data of *Samelson et al.* [2006] were collected at several locations along the channel, although the thickness of the floes moving through the Strait and the compactness of the ice field were not estimated in their study. The theoretical description developed in the present work provides predictions for the entire velocity profile across the channel width as well as the mean velocity, both of which rely on the ice properties (h, c) in addition to the geometry of the strait and the wind forcing. Here, we extract daily-averaged ice velocity and along-strait wind stress data from *Samelson et al.* [2006, Figure 2]. These data, which were obtained at a location where
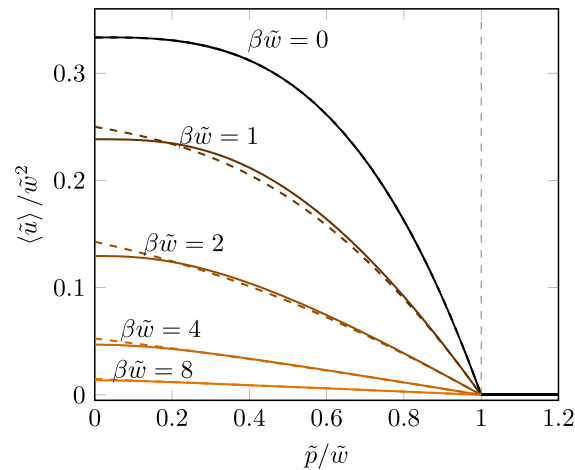
Figure 6. (a) Mean ice velocity versus the external stress f for different ice pressures p and drag coefficients β, showing excellent agreement of the approximate theory (43) (curves) with direct numerical simulations (symbols). Both the theory and the simulations assume a straight channel of half-width $w = 25$ km, uniform ice properties and a yield-curve eccentricity $\alpha = 2$; values of the other parameters are listed in Table 1. We assume fully compact ice ($c = 1$) so that $h = p/(Se^{-k(1-c)}) = p/S$ is a proxy for pressure, and plot results for $h = 0.5$ m (red, open symbols), $h = 1$ m (black, crossed symbols) and $h = 1.5$ m (blue, filled symbols). For each of these effective thicknesses, we present results for different values of the dimensionless linear drag parameter $\beta \equiv \sqrt{\alpha^2 w^2 \kappa_d / \zeta_{min}}$, here showing $\beta = 0$ (circles, solid curves), $\beta = 1$ (squares, dashed curves) and $\beta = 2$ (triangles, dotted curves). The present theory is applicable as long as the predicted ice velocities are smaller than the nominal free-drift velocity obtained from a quadratic drag law. (b) A rescaling of the results in Figure 6a, plotting the dimensionless mean ice velocity $\zeta_{min} \langle \bar{u} \rangle / (\alpha^2 w^2 f)$ as a function of the dimensionless forcing $\alpha w f / p$ for different values of β; symbols are results of a DNS and curves are the theoretical predictions of (43). The flow of ice only occurs for $f > p/(\alpha w)$, independent of the value of β.

the half-width of Nares Strait is $w \approx 23$ km, are compared with the theoretical prediction (42) for the mean velocity $\langle u \rangle$. Theoretical curves in Figure 7 correspond to different values of the pressure $p = She^{-k(1-c)}$, which, for convenience, are reported as inferred thickness values assuming $c = 1$. In more general situations with $c < 1$, as is likely the case in the measurements of *Samelson et al.* [2006] with flowing ice, a greater thickness is inferred for the same pressure ($h = pe^{k(1-c)}/S$). For example, with $c = 0.96$, the inferred thicknesses are about twice as large as those shown in Figure 7 for the parameters in Table 1. Thus, a one-to-one comparison with the data is difficult at present, in part due to the lack of simultaneous measurements of ice properties and forcing conditions.

A key feature of both the observations and the theory is that the ice can remain immobile even under a nonzero wind stress. Our theory quantifies this feature as a function of the ice pressure p, the channel width w, the strength of the forcing and the rheological parameter α: motion can only occur for $f > p/(\alpha w)$. For a forcing that exceeds this critical value, the ice velocity increases monotonically (provided that the ice properties and other relevant geometric and physical quantities remain constant) although its dependence on f and p is generally nonlinear.

We stress that the ice flow rate becomes zero for $p > \alpha w f$, independent of the value of β (see Figure 6b), due to the feature that there must always be a thin viscous layer near the walls in order for the flow to both satisfy the no-slip condition and support a plastic flow in the central region of the channel. Failure to establish such a layer, which occurs when $p > \alpha w f$, results in arrested flow. For large water drag ($\beta \gg 1$), although the value of ζ_{min} does not play a significant role in determining the flux or the velocity scale (see equations (42) and (43)), ζ_{min} is nonetheless essential to establishing the viscous layer, cf. section 3.1. Further, the inclusion of quadratic drag terms does not change the critical values of p for arrested flow, since these terms will approach zero more rapidly than the linear drag terms as $|\mathbf{u}| \to 0$.

The importance of the viscous layer in controlling the critical conditions for flow has not been discussed in detail in the literature. In addition, the role of ζ_{min} in determining the speed of the ice in the limit of small water drag appears to be largely unappreciated. Indeed, the parameter ζ_{min} was originally introduced by *Hibler* [1979] to avoid numerical instabilities. However, as we have shown here, a regularization (viscous or otherwise) of the plastic law is required on *physical* grounds if the no-slip condition is to be satisfied on the rigid boundaries that surround the ice flow. We further draw attention to the fact that the limiting ice viscosity ζ_{min} is usually taken to be a constant that is independent of the ice properties in most large scale climate models, which provides an unphysical resistance to flow in the limit of very thin or rarefied ice. A more sophisticated regularization of the plastic rheology in the weak-ice limit could, for example, involve a limiting viscosity that depends on the ice properties, or employ a relaxation of the no-slip condition in a way that depends on the ice strength. These are questions that warrant further attention but are beyond the focus of the present study. The analytical theory developed here can potentially be used to physically constrain the values of the model parameters, for example, S, ζ_{min} or k, based on measurements of fluxes and velocity profiles of sea ice flowing through straits.
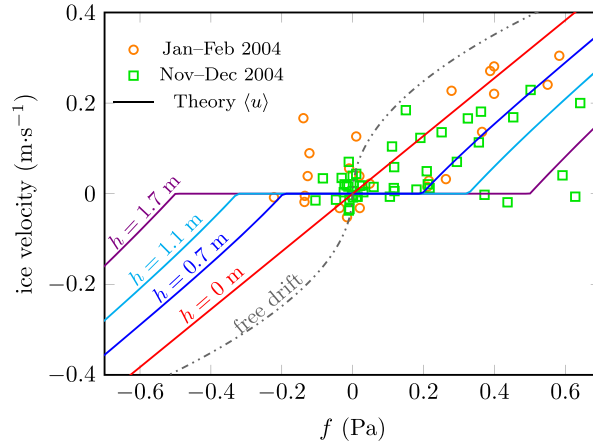
Figure 7. Ice velocity as a function of the wind stress, comparing the predictions of the present theory at a fixed drag coefficient κ_d (equation (43); solid curves) to the data of *Samelson et al.* [2006] (symbols) in Nares Strait. An ocean current estimate of 0.15 m·s^{-1} [*Samelson et al.*, 2006], with a width $w = 23$ km (characteristic of Nares Strait) and the rheological parameters in Table 1 yields $\kappa_d \approx 1$ Pa·s·m^{-1} ($\beta = 2.3$). The ice pressure $p = She^{-k(1-c)}$ is constant along each theoretical curve and is reported an effective value of h under the assumption that $c = 1$; note that $c < 1$ will result in a larger inferred mean thickness h for the same pressure. Positive wind stress corresponds to the predominant northerly wind in Nares Strait. Both the data and the theory indicate that ice only flows beyond a certain critical wind stress; the theory makes predictions for this critical wind stress. The scatter in the data can be attributed to uncertainties of ice thicknesses and ocean currents. On the other hand, the ice properties are crucial in determining the threshold minimum forcing for flow, making a one-to-one comparison challenging.

5. Conclusions

We have developed an analytical theory of sea ice flow in narrow straits that provides explicit quantitative predictions for the formation of ice bridges and the fluxes of sea ice. Our theory advances a systematic link between the properties of the ice encoded into its rheology, the geometry of the strait, and the external atmospheric and oceanic forcing conditions. We show that ice bridges can form only for a range of ice properties that depends on the external forcing on the ice and the maximum and minimum widths of the strait. We also calculate the flux of sea ice as a function of the properties of the ice and the geometry of the strait, and provide a simplified model for the evolution of these properties in time and space. The criteria for ice bridge formation were validated against direct numerical simulations. The predicted fluxes of sea ice for a straight channel reproduce results of the numerical simulations with excellent accuracy over a range of ice properties and forcing conditions, and are in general agreement with field observations.

The primary findings of the theory are encapsulated in (42), which not only predicts the mean ice velocity for a given forcing, but also carries the condition for arrested flow. The criterion (40) for the formation of ice arches in narrow straits of nonuniform shape relates the ice properties, the applied forcing and geometry of the strait.

The predictions for the fluxes obtained here can be used as inputs to GCMs in which resolving narrow straits is computationally infeasible. Incorporating these predictions of subgrid ice dynamics into GCMs may serve as a means to improve the modeling of ice export in large scale climate models with little to no additional computational cost. The analytical scalings developed here can potentially be used constrain model parameters based on physical measurements of flowing sea ice in straits. The incorporation of thermodynamic processes such as precipitation and phase change into the present framework will allow us to assess the seasonal stability of ice bridges.

Appendix A: Transverse Component of the Stress Balance

We briefly discuss the $\tilde{y}-$ component of the stress balance (29b) in the plastic flow region, which occurs for $|\tilde{y}| < \tilde{y}_v$. Rearranging (30) results in $\partial \tilde{u}_{p1}/\partial \tilde{y} = -(1 - \beta^2 \tilde{u}_p)\tilde{y}/\tilde{\eta}_p$, which can then be substituted into the (28) and the definition $\tilde{\eta}_p = \tilde{p}_p/\tilde{E}_p$ to obtain an algebraic equation that contains $\tilde{\eta}_p$, $\tilde{u}_p$, $\tilde{v}_p$, $\tilde{y}$ and $\tilde{p}_p$. Solving for $\tilde{\eta}_p$ then results in

$$\tilde{\eta}_p = \frac{\sqrt{\tilde{p}_p^2 - \tilde{y}^2(1 - \beta^2 \tilde{u}_p)^2}}{\sqrt{\left(\frac{\partial \tilde{u}_p}{\partial \tilde{x}} - \frac{\partial \tilde{v}_p}{\partial \tilde{y}}\right)^2 + \alpha^2 \left(\frac{\partial \tilde{u}_p}{\partial \tilde{x}} + \frac{\partial \tilde{v}_p}{\partial \tilde{y}}\right)^2}}. \tag{A1}$$

We note that (i) the above expression is only valid if $\tilde{p}_p(\tilde{x}, \tilde{y}) \geq \tilde{y}(1 - \beta^2 \tilde{u}_p)$, and (ii) $\tilde{\eta}_p$ involves $\partial \tilde{v}_p/\partial \tilde{y}$ which is yet unknown.

Further, (22b) can be integrated with respect to $\tilde{y}$ in a relatively straightforward manner. Recognizing that the normal stress must be continuous across the yield surface and that the normal stress in the viscous layer is equal to $-\alpha \tilde{p}_v$, we obtain the general expression

$$-\alpha\tilde{p}_p+\tilde{\eta}_p\left((\alpha^2-1)\frac{\partial\tilde{u}_p}{\partial\tilde{x}}+(\alpha^2+1)\frac{\partial\tilde{v}_p}{\partial\tilde{y}}\right)=-\alpha\tilde{p}_v(\tilde{x},\tilde{y})\,. \tag{A2}$$

Substituting the expression for $\tilde{\eta}_p$ results in a relation between $\tilde{p}_v$ and $\tilde{p}_p$ of the form

$$\tilde{p}_v(\tilde{x})=\tilde{p}_p-\sqrt{\tilde{p}_p^2-\tilde{y}^2(1-\beta^2\tilde{u}_p)^2}\left(\frac{(\alpha^2-1)\frac{\partial\tilde{u}_p}{\partial\tilde{x}}+(\alpha^2+1)\frac{\partial\tilde{v}_p}{\partial\tilde{y}}}{\alpha\sqrt{\left(\frac{\partial\tilde{u}_p}{\partial\tilde{x}}-\frac{\partial\tilde{v}_p}{\partial\tilde{y}}\right)^2+\alpha^2\left(\frac{\partial\tilde{u}_p}{\partial\tilde{x}}+\frac{\partial\tilde{v}_p}{\partial\tilde{y}}\right)^2}}\right). \tag{A3}$$

We recall that $\tilde{u}_p$ is known from (25) and (27), and that $\tilde{p}_v$ and $\tilde{p}_p$ depend on the ice properties $\tilde{h}$ and c in the viscous and plastic regions, respectively, although $\partial\tilde{v}_p/\partial\tilde{y}$ remains unknown. Defining

$$\chi(\tilde{x},\tilde{y})\equiv\frac{\tilde{p}_p-\tilde{p}_v}{\sqrt{\tilde{p}_p^2-\tilde{y}^2(1-\beta^2\tilde{u}_p)^2}}\,, \tag{A4}$$

we obtain upon squaring and rearranging (A3) that

$$(\alpha^2-1)\frac{\partial\tilde{u}_p}{\partial\tilde{x}}+(\alpha^2+1)\frac{\partial\tilde{v}_p}{\partial\tilde{y}}=\frac{2\chi\,\alpha^2\left|\frac{\partial\tilde{u}_p}{\partial\tilde{x}}\right|}{\sqrt{1-\alpha^2(\chi^2-1)}}, \tag{A5}$$

From (A5), we find

$$\frac{\partial\tilde{v}_p}{\partial\tilde{y}}=\frac{1}{\alpha^2+1}\frac{\partial\tilde{u}_p}{\partial\tilde{x}}\left(1-\alpha^2+\frac{2\chi\,\alpha^2\,\mathrm{sgn}\left(\frac{\partial\tilde{u}_p}{\partial\tilde{x}}\right)}{\sqrt{1-\alpha^2(\chi^2-1)}}\right), \tag{A6}$$

which depends on the pressure distribution.

The above expression (A6) can in principle be integrated for some given known pressure distributions $\tilde{p}_v$ and $\tilde{p}_p$. In the limit where the pressure across the channel is uniform $\tilde{p}_v=\tilde{p}_p$, we find from (A4) that $\chi=0$, which significantly simplifies (A6). Integrating in $\tilde{y}$ and applying the symmetry condition at $\tilde{y}=0$ results in

$$\tilde{v}_p(\tilde{x},\tilde{y})=-\frac{\alpha^2-1}{\alpha^2+1}\frac{\partial\tilde{u}_p}{\partial\tilde{x}}\tilde{y},\qquad\text{for}\quad\tilde{p}_v=\tilde{p}_p, \tag{A7}$$

thus determining of the transverse velocity in the plastic flow region. The general case of $\tilde{p}_v\neq\tilde{p}_p$ is significantly more complicated and affects the stress balance in the plastic-flow and the reduced-order system (35).

Appendix B: Wave Propagation in the Reduced-Order Model

We present a brief discussion of wave propagation in the system (36), which plays an important role in its evolution to steady state. In general, (36) can be written as a quasi-linear conservation law

$$\frac{\partial\boldsymbol{\phi}}{\partial\tilde{t}}+\frac{\partial\boldsymbol{\psi}}{\partial\tilde{x}}=\boldsymbol{0}\qquad\text{with}\quad 0\le c\le 1, \tag{B1}$$

where

$$\boldsymbol{\phi}(\tilde{x},\tilde{t})=\{\tilde{w}\tilde{h},\tilde{w}c\},\qquad\text{and}\quad\boldsymbol{\psi}(\tilde{x},\tilde{t})=\langle\tilde{u}\rangle\boldsymbol{\phi}\,. \tag{B2}$$

Although we solve this system numerically, it is useful to note some properties that allow the formation of ice bridges. We can rewrite the above system as

$$\frac{\partial\boldsymbol{\phi}}{\partial\tilde{t}}+\mathbf{J}\cdot\frac{\partial\boldsymbol{\phi}}{\partial\tilde{x}}+\left(\frac{\partial\boldsymbol{\psi}}{\partial\tilde{x}}\right)_{\boldsymbol{\phi}=\mathrm{const.}}=\boldsymbol{0}\,, \tag{B3}$$

where

$$\mathbf{J} = \left(\frac{\partial \boldsymbol{\psi}}{\partial \boldsymbol{\phi}}\right)_{\tilde{x}=const.} \tag{B4}$$

is the Jacobian matrix.

We consider the eigenvalue problem

$$\boldsymbol{\ell}^{(j)} \cdot \left(\mathbf{J} - \lambda^{(j)}\mathbf{I}\right) = \mathbf{0}, \quad \text{with} \quad j \in \{1, 2\} \tag{B5}$$

in which $\boldsymbol{\ell}^{(j)}$ are the left eigenvectors of $\mathbf{J}$ and $\lambda^{(j)}$ are the associated eigenvalues. Then, (B3) can be written as a system of two coupled ODEs along characteristic curves

$$\mathcal{C}^{(j)}: \quad \boldsymbol{\ell}^{(j)} \cdot \left(\frac{\mathrm{d}\boldsymbol{\varphi}}{\mathrm{d}\tilde{t}} + \left(\frac{\partial \boldsymbol{\psi}}{\partial \tilde{x}}\right)_{\varphi=const.}\right) = 0, \quad \text{on} \quad \frac{\mathrm{d}\tilde{x}^{(j)}}{\mathrm{d}\tilde{t}} = \lambda^{(j)}. \tag{B6}$$

Thus, the $\lambda^{(j)}$ are wave speeds at which information propagates along the characteristic curves $\mathcal{C}^{(j)}$.

When $\tilde{p} < \tilde{w}$, the Jacobian matrix is well defined. For example, in the limit $\beta = 0$ for which $\langle \tilde{u} \rangle$ is given by (38), the Jacobian admits the eigensystem

$$\lambda^{(1)} = \langle \tilde{u} \rangle, \quad \boldsymbol{\ell}^{(1)} = \left\{-c, \tilde{h}\right\}, \quad \text{and} \tag{B7a}$$

$$\lambda^{(2)} = \langle \tilde{u} \rangle - \tilde{w}^2(1+kc)\left(\frac{\tilde{h}\mathrm{e}^{-k(1-c)}}{\tilde{w}}\right)^3, \quad \boldsymbol{\ell}^{(2)} = \left\{1, k\tilde{h}\right\}. \tag{B7b}$$

Substituting the above expressions into (B6) results in the following system of characteristic equations

$$\mathcal{C}^{(1)}: \quad \frac{\mathrm{d}}{\mathrm{d}\tilde{t}}\left(\frac{c}{\tilde{h}}\right) = 0 \quad \text{on} \quad \frac{\mathrm{d}\tilde{x}^{(1)}}{\mathrm{d}\tilde{t}} = \lambda^{(1)} \quad \text{and} \tag{B8a}$$

$$\mathcal{C}^{(2)}: \quad \frac{1}{\tilde{p}}\frac{\mathrm{d}\tilde{p}}{\mathrm{d}\tilde{t}} = \frac{1}{\tilde{h}}\frac{\mathrm{d}\tilde{h}}{\mathrm{d}\tilde{t}} + k\frac{\mathrm{d}c}{\mathrm{d}\tilde{t}} = -(1+kc)\tilde{w}\frac{\mathrm{d}\tilde{w}}{\mathrm{d}\tilde{x}} \quad \text{on} \quad \frac{\mathrm{d}\tilde{x}^{(2)}}{\mathrm{d}\tilde{t}} = \lambda^{(2)}, \tag{B8b}$$

where we have used the chain rule to write $\mathrm{d}\tilde{w}/\mathrm{d}\tilde{t} = (\mathrm{d}\tilde{w}/\mathrm{d}\tilde{x})(\mathrm{d}\tilde{x}^{(2)}/\mathrm{d}\tilde{t})$ along $\mathcal{C}^{(2)}$ in order to obtain (B8b). However, if $\tilde{p} > \tilde{w}$, we find $\boldsymbol{\psi} = \mathbf{0}$, independent of the precise values of $\tilde{h}$ and c. As a result, the system becomes degenerate, i.e., $\mathbf{J} = \partial \boldsymbol{\psi}/\partial \boldsymbol{\phi} = \mathbf{0}$, and has vanishing wave speeds

$$\lambda^{(1)} = \lambda^{(2)} = 0. \tag{B9}$$

Thus, regions of the flow in which $\tilde{p} > \tilde{w}$ are opaque to wave propagation. We remark that the wave speeds (in particular $\lambda^{(2)}$) are discontinuous around $\tilde{p} = \tilde{w}$.

In the results presented in Figure 3b, no information can propagate across the initial blockage (the region between the dashed lines), effectively isolating the ice fields on either side of the blockage. By contrast, the ice field in Figure 3a is initially such that $\tilde{p} < \tilde{w}$, so that its wave speeds vary continuously with $\tilde{h}$ and c. The vanishing of these wave speeds for $\tilde{p} > \tilde{w}$ ensures that local regions that are initially arrested isolate different parts of the flow. This behavior is essential for the formation of a discontinuous steady-state solution in the reduced-order model, such as the one indicated in Figures 3b and 3c.

In the case where $\tilde{p} < \tilde{w}$, we note from (B8) that the $\mathcal{C}^{(1)}$ set of characteristics always propagates rightward with the mean flow velocity, and the $\mathcal{C}^{(2)}$ characteristics can propagate either leftward or rightward depending on the values of $\tilde{h}$ and c. We also observe from (B8b) that pressure waves propagate on $\mathcal{C}^{(2)}$ characteristics; the pressure decreases if the channel widens in the direction of wave propagation, and increases if the channel narrows in the direction of wave propagation. The speed and direction of these waves depend on $\tilde{h}$, c and $\tilde{w}$, so the resulting evolution of $\tilde{p}$ is nontrivial and will generally involve shock and rarefaction phenomena.

References

Balmforth, N. J., and R. V. Craster (1999), A consistent thin-layer theory for Bingham plastics, *J. Non-Newton Fluid. Mech.*, *84*(1), 65–81.

Bird, R. B., R. C. Armstrong, O. Hassager, and C. F. Curtiss (1977), *Dynamics of Polymeric Liquids*, vol. 1, John Wiley, New York.

Bowman, J. P., and R. D. McCuaig (2003), Biodiversity, community structural shifts, and biogeography of prokaryotes within Antarctic continental shelf sediment, *Appl. Environ. Microbiol.*, *69*(5), 2463–2483.

Coon, M., R. Kwok, G. Levy, M. Pruis, H. Schreyer, and D. Sulsky (2007), Arctic Ice Dynamics Joint Experiment (AIDJEX) assumptions revisited and found inadequate, *J. Geophys. Res.*, *112*, C11S90, doi:10.1029/2005JC003393.

Coon, M. D., G. A. Maykut, and R. S. Pritchard (1974), Modeling the pack ice as an elastic-plastic material, *AIDJEX Bull.*, *24*, 1–105.

Dansereau, V., J. Weiss, P. Saramito, and P. Lattes (2016), A Maxwell elasto-brittle rheology for sea ice modelling, *Cryosphere*, *10*(3), 1339–1359.

Dumont, D., Y. Gratton, and T. E. Arbetter (2009), Modeling the dynamics of the North Water Polynya ice bridge, *J. Phys. Oceanogr.*, *39*(6), 1448–1461.

Feltham, D. L. (2008), Sea ice rheology, *Annu. Rev. Fluid Mech.*, *40*, 91–112.

Forterre, Y., and O. Pouliquen (2008), Flows of dense granular media, *Annu. Rev. Fluid Mech.*, *40*, 1–24.

Frigaard, I. A., and D. P. Ryan (2004), Flow of a visco-plastic fluid in a channel of slowly varying width, *J. Non-Newton Fluid. Mech.*, *123*(1), 67–83.

Harten, A., P. D. Lax, and B. van Leer (1983), On upstream differencing and Godunov-type schemes for hyperbolic conservation laws, *SIAM Rev.*, *25*(1), 35–61.

Henann, D. L., and K. Kamrin (2013), A predictive, size-dependent continuum model for dense granular flows, *Proc. Natl. Acad. Sci. U. S. A.*, *110*(17), 6730–6735.

Hibler, W. D., III (1977), A viscous sea ice law as a stochastic average of plasticity, *J. Geophys. Res.*, *82*(27), 3932–3938.

Hibler, W. D., III (1979), A dynamic thermodynamic sea ice model, *J. Phys. Oceanogr.*, *9*(4), 815–846.

Hibler, W. D., III (2001), Sea ice fracturing on the large scale, *Eng. Fracture Mech.*, *68*(17), 2013–2043.

Hibler, W. D., III., J. K. Hutchings, and C. F. Ip (2006), Sea-ice arching and multiple flow states of arctic pack ice, *Ann. Glaciol.*, *44*(1), 339–344.

Hobson, K. A., A. Fisk, N. Karnovsky, M. Holst, J.-M. Gagnon, and M. Fortier (2002), A stable isotope (δ^{13}C, δ^{15}N) model for the North Water food web: Implications for evaluating trophodynamics and the flow of energy and contaminants, *Deep Sea Res., Part II*, *49*(22), 5131–5150.

Howell, S. E. L., F. Laliberté, R. Kwok, C. Derksen, and J. King (2016), Landfast ice thickness in the Canadian Arctic Archipelago from observations and models, *Cryosphere*, *10*(4), 1463–1475, doi:10.5194/tc-10-1463-2016.

Hunke, E. C. (2001), Viscous–plastic sea ice dynamics with the EVP model: Linearization issues, *J. Comput. Phys.*, *170*(1), 18–38.

Hunke, E. C., and J. K. Dukowicz (1997), An elastic-viscous-plastic model for sea ice dynamics, *J. Phys. Oceanogr.*, *27*(9), 1849–1867.

Ip, C. F., W. D. Hibler III, and G. M. Flato (1991), On the effect of rheology on seasonal sea-ice simulations, *Ann. Glaciol.*, *15*(1), 17–25.

Jop, P., Y. Forterre, and O. Pouliquen (2006), A constitutive law for dense granular flows, *Nature*, *441*(7094), 727–730.

Kwok, R. (2005), Variability of Nares Strait ice flux, *Geophys. Res. Lett.*, *32*, L24502, doi:10.1029/2005GL024768.

Kwok, R. (2006), Exchange of sea ice between the Arctic Ocean and the Canadian Arctic Archipelago, *Geophys. Res. Lett.*, *33*, L16501, doi:10.1029/2006GL027094.

Kwok, R., L. Toudal Pedersen, P. Gudmandsen, and S. S. Pang (2010), Large sea ice outflow into the Nares Strait in 2007, *Geophys. Res. Lett.*, *37*, L03502, doi:10.1029/2009GL041872.

Leppäranta, M. (2011), *The Drift of Sea Ice*, Springer Sci. & Business Media, Heidelberg.

LeVeque, R. J. (2002), *Finite Volume Methods for Hyperbolic Problems*, vol. 31, Cambridge Univ. Press, Cambridge, U. K.

Marsden, R. F., J. Serdula, E. Key, and P. J. Minnett (2004), Are polynyas self-sustaining?, *Atmos. Oceans*, *42*(4), 251–265.

McPhee, M. G. (1975), Ice-ocean momentum transfer for the AIDJEX ice model, *AIDJEX Bull.*, *29*, 93–111.

Melling, H. (2002), Sea ice of the northern Canadian Arctic Archipelago, *J. Geophys. Res.*, *107*(C11), 3181, doi:10.1029/2001JC001102.

Ockendon, H., and J. R. Ockendon (1995), *Viscous Flow, Cambridge Texts Appl. Math.*, Cambridge Univ. Press, Cambridge, U. K.

Overland, J. E., and C. H. Pease (1988), Modeling ice dynamics of coastal seas, *J. Geophys. Res.*, *93*(C12), 15,619–15,637.

Rabatel, M., S. Labbé, and J. Weiss (2015), Dynamics of an assembly of rigid ice floes, *J. Geophys. Res. Oceans*, *120*, 5887–5909, doi:10.1002/2015JC010909.

Rallabandi, B., Z. Zheng, M. Winton, and H. A. Stone (2017), Wind-driven formation of ice bridges in straits, *Phys. Rev. Lett.*, *118*, 128,701.

Richmond, O., and G. C. Gardner (1962), Limiting spans for arching of bulk materials in vertical channels, *Chem. Eng. Sci.*, *17*(12), 1071–1078.

Rothrock, D. A. (1975a), The mechanical behavior of pack ice, *Annu. Rev. Earth Planet. Sci.*, *3*(1), 317–342.

Rothrock, D. A. (1975b), The steady drift of an incompressible Arctic ice cover, *J. Geophys. Res.*, *80*(3), 387–397.

Ryan, P. A., and A. Münchow (2017), Sea ice draft observations in Nares Strait from 2003 to 2012, *J. Geophys. Res. Oceans*, *122*, 3057–3080, doi:10.1002/2016JC011966.

Samelson, R. M., T. Agnew, H. Melling, and A. Münchow (2006), Evidence for atmospheric control of sea-ice motion through Nares Strait, *Geophys. Res. Lett.*, *33*, L02506, doi:10.1029/2005GL025016.

Scambos, T., H. A. Fricker, C.-C. Liu, J. Bohlander, J. Fastook, A. Sargent, R. Massom, and A.-M. Wu (2009), Ice shelf disintegration by plate bending and hydro-fracture: Satellite observations and model results of the 2008 Wilkins ice shelf break-ups, *Earth Planet. Sci. Lett.*, *280*(1), 51–60.

Schulson, E. M. (2004), Compressive shear faults within arctic sea ice: Fracture on scales large and small, *J. Geophys. Res.*, *109*, C07016, doi:10.1029/2003JC002108.

Smith, R. B. (1983), A note on the constitutive law for sea ice, *J. Glaciol.*, *29*(101), 191–195.

Sodhi, D. S. (1977), Ice arching and the drift of pack ice through restricted channels, *CRREL Rep.*, *77–18*, Cold Regions Research and Engineering Laboratory, Hanover, N. H.

Stelma, S. A. (2015), The effects of atmospheric and oceanic conditions on the stability of ice bridges, Master's thesis, Univ. of Delaware, Newark, Delaware.

Stirling, I. (1997), The importance of polynyas, ice edges, and leads to marine mammals and birds, *J. Mar. Syst.*, *10*(1), 9–21.

Thorndike, A. S., D. A. Rothrock, G. A. Maykut, and R. Colony (1975), The thickness distribution of sea ice, *J. Geophys. Res.*, *80*(33), 4501–4513.

Tichy, J. A. (1991), Hydrodynamic lubrication theory for the Bingham plastic flow model, *J. Rheol.*, *35*(4), 477–496.

Toppaladoddi, S., and J. S. Wettlaufer (2015), Theory of the sea ice thickness distribution, *Phys. Rev. Lett.*, *115*, 148,501.

Tremblay, L. B., and L. A. Mysak (1997), Modeling sea ice as a granular material, including the dilatancy effect, *J. Phys. Oceanogr.*, *27*(11), 2342–2360.

Trenberth, K. E. (1992), *Climate System Modeling*, Cambridge Univ. Press, Cambridge, U. K.

Wilchinsky, A. V., and D. L. Feltham (2004), Dependence of sea ice yield-curve shape on ice thickness, *J. Phys. Oceanogr.*, *34*(12), 2852–2856.

Wilchinsky, A. V., and D. L. Feltham (2006), Modelling the rheology of sea ice as a collection of diamond-shaped floes, *J. Non-Newton Fluid Mech.*, *138*(1), 22–32.

Wilchinsky, A. V., and D. L. Feltham (2011), Modeling Coulombic failure of sea ice with leads, *J. Geophys. Res.*, *116*, C08040, doi:10.1029/2011JC007071.

Worster, M. G., and D. W. Rees Jones (2015), Sea-ice thermodynamics and brine drainage, *Philos. Trans. R. Soc. A*, *373*(2045), 20140,166.

Zhang, J., and D. A. Rothrock (2005), Effect of sea ice rheology in numerical investigations of climate, *J. Geophys. Res.*, *110*, C08014, doi:10.1029/2004JC002599.